water

MDPI

Review

Spinel-Ferrite-Decorated Graphene-Based Nanocomposites for Enhanced Photocatalytic Detoxification of Organic Dyes in Aqueous Medium: A Review

Subhasish Mishra [1], Rashmi Acharya [1,*] and Kulamani Parida [2]

[1] Department of Chemistry, Institute of Technical Education and Research, Siksha 'O' Anusandhan Deemed to be University, Bhubaneswar 751030, Odisha, India
[2] Centre for Nano Science and Nano Technology, Institute of Technical Education and Research, Siksha 'O' Anusandhan Deemed to be University, Bhubaneswar 751030, Odisha, India
* Correspondence: drrashmiacharya75@gmail.com or rashmiacharya@soa.ac.in; Tel.:+91-674-2350-181 or 91-674-2351538; Fax: +91-674-2350-642

Abstract: The contamination of organic dye molecules in aquatic environments caused by the effluents released from vast industrial establishments has been a matter of serious concern in recent years, owing to their strong non-biodegradable nature and acute toxicity. Semiconductor-mediated visible-light-driven photocatalytic-dye detoxification is considered as a sustainable technique because it abundantly utilizes the available solar energy and releases environmentally friendly chemicals such as H_2O as byproducts. Adequate textural and microstructural properties, an extended visible-light response, pronounced isolation and transfer of photoinduced charge carriers, and facile magnetic-separation characteristics make spinel-ferrite-decorated graphene or its analogues' (GO/rGO) nanocomposites (MFGNs) a versatile photocatalytic system for the efficacious detoxification of dyes. Therefore, this review article emphasizes their exceptional photodegradation performance in terms of systematic studies of the above-mentioned features, after a brief description of the synthesis protocols. The mechanism of the photodetoxification of dyes over MFGNs is precisely demonstrated in three different sections based on their redox abilities. The kinetics of the MFGN-driven photodecomposition of dyes are then highlighted. We discuss the role of different parameters such as pH, temperature, catalyst dose, and dye concentration in augmented photocatalytic-dye-degradation reactions. Finally, the emerging challenges that act as hurdles in achieving superior photocatalytic-dye-detoxification performance are addressed, along with the conclusion. We then propose some possible future research directions in order to overcome these challenges, for impressively accomplishing the photodegradation of organic dyes.

Keywords: photocatalytic detoxification; organic dyes; textural properties; charge carriers' separation; light absorption range; facile recoverability

Citation: Mishra, S.; Acharya, R.; Parida, K. Spinel-Ferrite-Decorated Graphene-Based Nanocomposites for Enhanced Photocatalytic Detoxification of Organic Dyes in Aqueous Medium: A Review. *Water* **2023**, *15*, 81. https://doi.org/10.3390/w15010081

Academic Editors: Jiangyong Hu, Say Leong Ong, Guangli Liu and Yongjun Zhang

Received: 22 November 2022
Revised: 16 December 2022
Accepted: 20 December 2022
Published: 26 December 2022

1. Introduction

Water is the most vital and essential component for the survival of living organisms. The use of safe and clean water leads to a healthier life. However, massive establishments in industries such as paper, pigments, textiles, apparel, etc., discharge substantial amount of dye-containing effluents into natural aqueous ecosystems [1,2]. It has been reported that 10–12% of dyes are used in textile industries every year, out of which 20% are released in the form of waste water into nearby water bodies. According to a World Bank report, 17–20% of water pollution is caused by the effluents from the dyeing and textile industries. The Ecological and Toxicological Association of the Dyestuffs Manufacturing Industry (ETAD) reported that 90% of the tested 4000 dyes exhibited a medial lethal dose (LD_{50}) of greater than 2×10^3 mg kg^{-1}. Being strongly non-biodegradable, these organic molecules freely enter into the human body and pose serious ailments owing to their acute

toxicity [3]. Therefore, it has been a challenge for the scientific community to eradicate these noxious substances from aquatic environments. Various techniques including adsorption, membrane separation, ion exchange, coagulation, etc., have been employed to remove these dyes from water and waste water [4–6]. Although the adsorption process has been widely adopted for the removal of dyes due to its cost effectiveness and ease of operation, its practical application is greatly restricted by several bottlenecks such as a prolonged desorption period, the generation of secondary pollutants, and the incomplete removal of dyes [7]. In contrast, the photocatalytic degradation of dyes over a semiconductor's surface under visible light irradiation has been garnering excitement in recent years, as it completely decomposes dye molecules into harmless products such as H_2O and CO_2 [8,9].

Semiconductor-mediated photocatalytic-dye degradation is being extensively investigated after the pioneering work of Frank and Bard on the photocatalytic oxidation of CN^- in water over a series of semiconductors under light irradiation [10]. The fundamental mechanism of semiconductor-based photocatalytic-dye detoxification proceeds through three crucial steps (Scheme 1). Step I involves the absorption of photon fluxes with energy higher than or equal to the band gap of the semiconductor, followed by the production of electron–hole pairs. Step II accounts for the separation and transfer of these photoinduced excitons. In step III, the photon-produced charge carriers undergo redox reactions to release highly reactive species such as superoxide anions ($O_2^{\bullet-}$) and hydroxyl free radicals ($HO^\bullet$), which are responsible for the decomposition of dyes. In some cases, holes (h^+) also participate in the degradation reaction [11,12]. However, the possibility of the recombination of the photon-produced excitons cannot be neglected. The efficiency of a semiconductor photocatalyst relies on its redox ability and the availability of charge carriers on its surface. Numerous semiconducting photocatalysts, namely TiO_2, CeO_2, ZnO, etc., have been applied for the photodegradation of dyes. Their poor visible-light-absorption capability fails to produce the required number of charge carriers under solar energy irradiation [13–15]. Usually, the visible-light-absorption capacity of a semiconductor is the prerequisite to achieve the required number of charge carriers. Subsequently, visible-light-responsive semiconductors such as CdS, g-C_3N_4, $BiVO_4$, etc., are used to harness solar energy in order to produce a higher number of electron–hole pairs. Nevertheless, the high rate of charge carriers' recombination led them to exhibit poor photocatalytic performance regarding dye decomposition [16,17]. In addition, difficulties in the separation of these photocatalysts from a treated solution made the downstream processing tedious [18]. In this context, the search for a suitable photocatalytic system with an extended visible-light-absorption ability, a pronounced charge carriers' isolation and transportation capability, and a good recoverable affinity are highly desirable.

Contrastingly, spinel ferrites with appreciable magnetic properties can facilely be separated from an aqueous environment under the influence of an external magnetic field. Their narrow band gap energy, required band edge positions, facile fabrication techniques, enlarged surface area, reasonable stability, and low cost have persuaded the research community to utilize them in versatile applications in the visible-light-induced photocatalytic-dye-degradation process [19]. Spinel ferrites are categorized as homogenous materials with the general formula MFe_2O_4 (MF). M represents doubly positively charged metal ions, and Fe exists as Fe^{3+}. The M^{2+} ions are placed at the tetrahedral crystallographic sites, while the Fe^{3+} ions occupy the octahedral crystallographic sites. The structure of the ferrites mostly depends on the arrangement of the Fe^{3+} and M^{+2} ions on both of the crystallographic sites. Spinel ferrite is a closely packed oxide structure where the oxide ions are in an FCC arrangement. In a normal spinel structure, the M^{2+} ions occupy the tetrahedral sites, whereas the octahedral sites are utilized by Fe^{3+} ions. For example, $ZnFe_2O_4$ crystallizes with a normal spinel structure, in which the Zn^{2+} and Fe^{3+} ions occupy the tetrahedral and octahedral sites, respectively. In an inverse spinel structure, the Fe^{3+} ions are equally distributed between the tetrahedral and octahedral sites, and the M^{2+}

ions occupy the remaining half of the octahedral sites. Ferrites such as $NiFe_2O_4$, $CoFe_2O_4$, etc., possess inverse spinel structures [20,21].

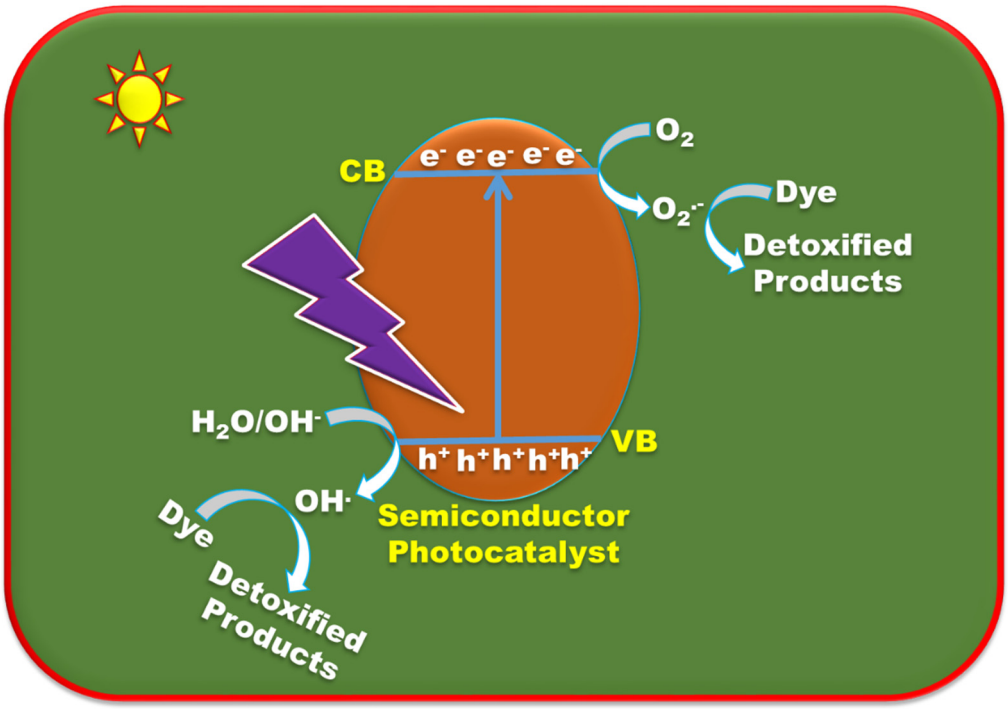

Scheme 1. Fundamental mechanism of photocatalytic-dye detoxification over a semiconductor photocatalyst.

Notwithstanding several advantageous features, the photoactivity of MFs lies far away from the expectations, mainly due to the poor charge carriers' separation and narrow visible-light-responsive window. In order to overcome these impediments, MFs are composited with 2D nanomaterials such as graphene as well as its derivatives GO and rGO (GN). The robust interaction between the two, with a retention of structure and properties, is very much crucial for augmented photocatalytic performance [22,23]. This can be achieved by adopting suitable synthesis protocols and can be confirmed through various characterization techniques. GNs have a π-conjugated electronic structure with an ultrafast electron-transfer ability, which facilitates the isolation and transportation of the photoinduced electrons from the MF surface upon thorough interaction. Concurrently, the recombination of electron and hole pairs is significantly inhibited, and the MF-decorated GN exhibits ameliorated photocatalytic performance [24]. Furthermore, the effective combination of GN with MFs extends the visible-light-absorption range to a longer wavelength region. In addition, the firm adherence of MF materials significantly improves MFGNs' microstructural and textural properties, which facilitate the effective adsorption of dye molecules for efficient catalytic reactions. Owing to these auspicious advantages, MFGNs have been investigated in diversified fields of photocatalysis including energy generation and environmental remediation. The Wang group synthesized $ZnFe_2O_4$/graphene composites for the photocatalytic degradation of methylene blue (MB) in 2011. They successfully achieved 90% MB detoxification within 90 min of visible light exposure [25]. Hou et al. reported that 91.4% photodegradation of p-chlorophenol was obtained by $ZnFe_2O_4$/graphene composites [26]. Behera et al. fabricated a $ZnFe_2O_4$/rGO system for photocatalytic water splitting and ciprofloxacin degradation. This MFGN system was able to produce 410.32 μmol/h of H_2 via water splitting and perform 73% ciprofloxacin degradation under visible-light irradiation [27]. In another study, 28.8 μmol/(L·cm^2) methanol was produced by the photocatalytic conversion of CO_2 over $CuFe_2O_4$/GO composites. The amount of methanol formed by the composite was 1.9 times greater than that of pristine $CuFe_2O_4$ [28]. However, extensive research has

been carried out in the field of photocatalytic-dye detoxification using MFGNs to date. Therefore, it is of great scientific significance to summarize the photocatalytic performance of MFGN composites regarding the degradation of organic dyes.

In this review, the synthesis protocols for the preparation of MFGN composites are depicted. Further, we address the enhanced photocatalytic performance of these composites in terms of improved textural and microstructural properties, comprehensive charge carriers' separation and migration, and magnified-light-response affinity. The kinetics and mechanism of the photogradation of dyes over MFGNs are discussed. The factors affecting photocatalytic performance over MFGN composites for dye degradation are briefly illustrated. The enhanced stability and facile recoverability of these classes of composites are depicted thoroughly. We then compare the dye-degradation ability of MFGNs with MFs. In conclusion, some of the advantages of the present system in exhibiting impressive performance regarding the photodestruction of organic dye molecules are depicted. At the end, we highlight the challenges that prevent the expected performance of MFGNs for photocatalytic-dye detoxification. The future research directions are then highlighted, with an objective of overcoming the persisting challenges for enhancing the photocatalytic-dye-detoxification capability of MFGNs.

2. Synthesis Protocols

Synthesis strategies have a great impact on the morphology, structure, and composition of nanocomposites. Thus, a well-organized synthesis protocol can help in achieving nanocomposites with better crystallinity, optimum particle size, and desired microstructure, which eventually leads to peerless photocatalytic activity [29]. Spinel-ferrite-decorated graphene-based nanocomposites (MFGNs) are synthesized via different processes such as solvothermal, hydrothermal, co-precipitation, sol–gel, and ball milling. Fei et al. reported a one-step solvothermal method to synthesize magnetic rGO/$ZnFe_2O_4$. They used $ZnCl_2$, $FeCl_3 \cdot 6H_2O$, and GO as the precursors, with ethylene glycol as the solvent. The mixture was then autoclaved at 200 °C for 24 h to obtain the desired product. The strong and sharp diffraction peaks, as shown in the XRD pattern (Figure 1a), resembles those of the cubic $ZnFe_2O_4$ well [30]. This confirms that the zinc ferrite in the composite retains crystallinity. The disappearance of the (002) peak at $2\theta = 26.2°$ corresponding to the graphite (Figure 1a) in the composite, indicated the destruction of the regular stacking of the rGO sheets in the presence of $ZnFe_2O_4$ nanoparticles. Solvothermal methods were also used to prepare the rGO/$CoFe_2O_4$ nanohybrid, using $FeCl_3 \cdot 6H_2O$ and $CoCl_2 \cdot 6H_2O$ as the precursors in a mixture of ethylene glycol and deionized water. With the addition of GO dispersion, the prepared solution was stirred and autoclaved at 180 °C for 12 h. The obtained composite was analyzed by XPS, as shown in Figure 1b. Intense Co $2P_{3/2}$ peaks with binding energy at 780.5 and 786.4 eV confirmed the presence of Co^{2+} species in the composite. Likewise, Fe 2P level with binding energy at 711.4 eV and 724.5 eV corresponding to Fe $2P_{3/2}$ and Fe $2P_{1/2}$, respectively, confirmed the presence of Fe^{3+} ions in the composite. The presence of C 1s spectrum indicated surface functionalities in the composite. Combining all these pieces of evidence, it was confirmed that the $CoFe_2O_4$ nanoparticles were anchored firmly on the surface of the graphene nanosheets [31]. The Ai group was manifested from the SEM micrographs (Figure 1c) that solvothermally fabricated the $CoFe_2O_4$/rGO nanocomposites, which possessed intimate interfacial contact between the $CoFe_2O_4$ nanoparticles and rGO sheets [32]. Meidinchi and co-authors synthesized $ZnFe_2O_4$/rGO by a hydrothermal method. The aqueous mixture of $Zn(NO_3)_2$, $Fe(NO_3)_3$, and GO powder was subjected to hydrothermal treatment at 180 °C for 12 h to obtain the desired product. The Raman spectra of these samples are shown in Figure 1d. The G band and D band appeared near 1595 cm^{-1} and at 1353 cm^{-1}, respectively, indicating the presence of GO. The I_g/I_d ratio for GO was found to be 0.77, while that for $ZnFe_2O_4$/rGO decreased to 0.54. This decrease in the I_g/I_d ratio indicated the presence of chemical bonds between the $ZnFe_2O_4$ nanoparticles and rGO. This confirmed the successful formation of the $ZnFe_2O_4$/rGO composite [33]. $MnFe_2O_4$/GO nanohybrids were reportedly synthesized

by the co-precipitation method using $FeCl_3$, $MnSO_4$, and an aqueous graphene oxide solution. The mixture solution was subjected to stirring at 80 °C, and then the pH of the mixture was adjusted to 10.5 by adding the required volume of a NaOH solution. The nanohybrids obtained were characterized by Fourier Transform Infra-Red (FTIR) spectra. The absorption peaks at 490 $cm^{-1}$and 577 cm^{-1} corresponded to the metal–oxygen bond stretching vibrations, which confirmed the formation of $MnFe_2O_4$ nanoparticles. Bands at 1044 cm^{-1}, 1236 cm^{-1}, 1415 cm^{-1}, and 1620 cm^{-1} corresponded to GO (Figure 1e). This information helped in support of the successful formation of a $MnFe_2O_4$/GO composite [34]. Rostami et al. prepared $ZnFe_2O_4$/graphene nanohybrids via the sol–gel method using $Zn(NO_3)_2{\cdot}6H_2O$, $FeCl_3{\cdot}6H_2O$, and citric acid as precursors. The molar ratio of cations to citric acid was maintained at 1:2. SEM studies of a $ZnFe_2O_4$/graphene composite revealed that $ZnFe_2O_4$ nanocrystals with an 85–95 nm diameter were decorated with exfoliated graphene nanosheets [35]. The ball milling technique was also used to prepare $CoFe_2O_4$/rGO nanohybrids. In a typical experiment, a mixture containing a predetermined amount of cobalt and iron precursors along with a given amount of GO colloid was adjusted to pH 10 by adding NH_3 and then was milled with an oscillation of 25 s^{-1} for 6 h to obtain $CoFe_2O_4$/rGO. It was observed from the TEM image shown in Figure 1f that $CoFe_2O_4$ nanoparticles with a 10 to 15 nm size are evenly distributed over exfoliated and wrinkled graphene nanosheets [36].

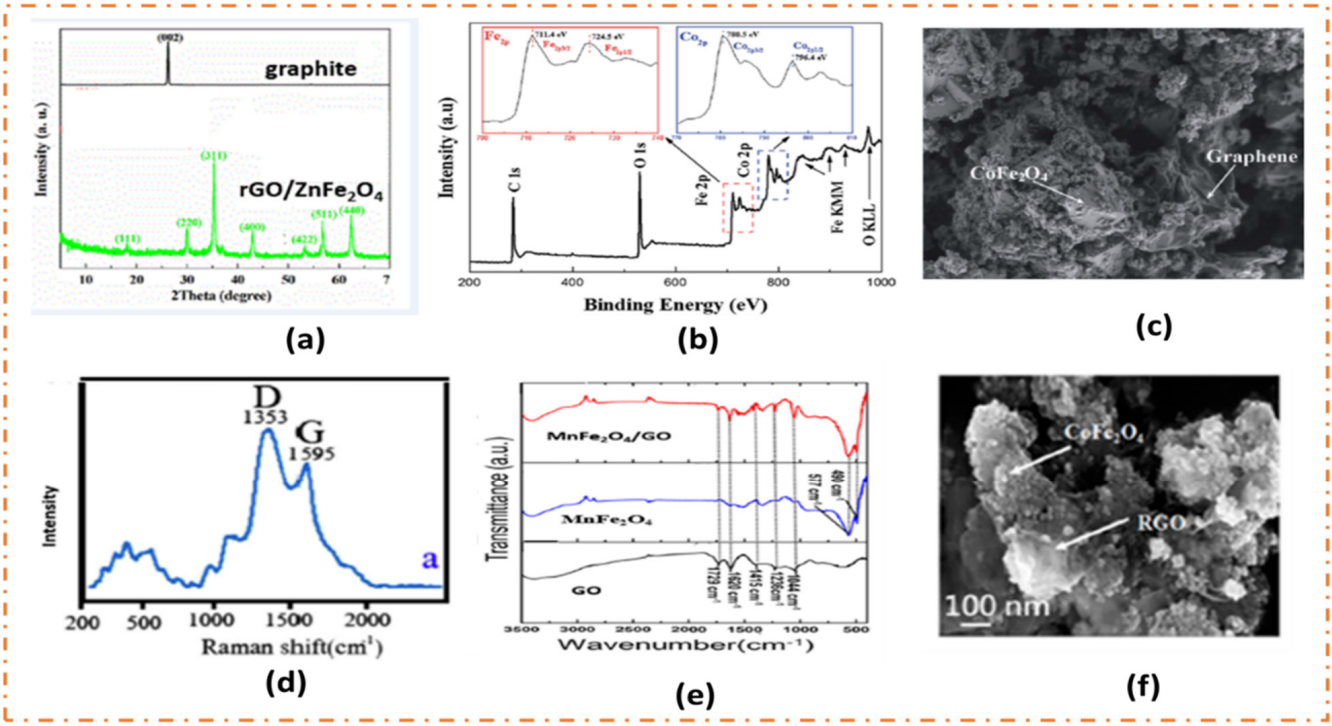

Figure 1. (**a**) XRD patterns for graphite and rGO/$ZnFe_2O_4$ "Reprinted/adapted with permission from Ref. [30]. 2016, Elsevier". (**b**) XPS analysis of rGO/$CoFe_2O_4$ "Reprinted/adapted with permission from Ref. [31]. 2017, RSC" (**c**) FESEM images of $CoFe_2O_4$/graphene composite showing firm adhesion between pristine SF and graphene "Reprinted/adapted with permission from Ref. [32]. 2021, RSC". (**d**) Raman spectra of $ZnFe_2O_4$/rGO "Reprinted/adapted with permission from Ref. [33]. 2014, Elsevier". (**e**) FTIR data for $MnFe_2O_4$, GO/$MnFe_2O_4$ composite, and GO "Reprinted/adapted with permission from Ref. [34]. 2014, ACS". (**f**) TEM image for rGO/$CoFe_2O_4$ "Reprinted/adapted with permission from Ref. [36]. 2015, ACS".

3. Role of Decoration of Spinel Ferrites on Graphene in MFGN for Enhanced Photocatalytic-Dye Detoxification

MFGNs show enhanced photocatalytic activity mainly due to three factors. Firstly, the π-conjugated electronic structure of GN acts as an efficient electron acceptor and transporter. Photogenerated electrons can readily be transferred to the GN surface owing to its higher work function [37,38]. Thus, the presence of GN in the MFGN composites can readily decrease the electron–hole pair recombination, and the photoinduced charge carriers are distinctly available to carry out redox reactions. Secondly, graphene plays a pivotal role in extending the light-absorption range of MF to the red end of the visible region [39]. As a result, MFGN becomes able to harness a larger amount of solar radiation, which is an indispensable aspect of augmented photoactivity. Moreover, the 2D structure of graphene enables MFGN to possess an enlarged surface area, enhanced pore structure, and adequate morphology, which are advantageous for acquiring abundant active surface sites. Theses active sites adsorb the organic dye molecules effectively for efficient photodegradation. In this section, we describe these aspects in detail.

3.1. Textural and Microstructural Properties of MFGN

The surface properties of MFGNs play an important role in the adsorption of pollutants. A large specific surface area, smaller particle size, and distinct porous structure help in the adsorption of the organic dyes over the MFGN surface. This ultimately leads to ameliorated photocatalytic activity. As shown in the FESEM image (Figure 2a) of the $CoFe_2O_4$/rGO composite, $CoFe_2O_4$ nanoparticles were homogenously anchored on the wrinkled rGO surface. The rGO loading led to a decrease in the agglomeration of $CoFe_2O_4$ along with a reduction in its particle size, from 58 nm to 49 nm. As a result, rGO-loaded $CoFe_2O_4$ exhibited 1.3 times more Methylene blue (MB) photodegradation under visible-light illumination compared to bare $CoFe_2O_4$ nanoparticles [40]. Baynosa et al. demonstrated that the improved textural properties of $ZnFe_2O_4$/rGO nanocomposites are responsible for the boosted photodetoxification of MB. They observed from the BJH-adsorption pore-size distribution curves that the average pore diameter for $ZnFe_2O_4$ was 12.4 nm (Figure 2b), while that of the $ZnFe_2O_4$/rGO nanocomposite was only 5.2 nm (Figure 2c). Furthermore, the hybridization of rGO with $ZnFe_2O_4$ has made a quantum leap in specific surface area, from the 113.8 $m^2\ g^{-1}$ observed for pristine $ZnFe_2O_4$ (Figure 2d) to 141.3 $m^2\ g^{-1}$ (Figure 2e). The improved textural properties of the composite photocatalyst possessed a higher number of active sites, which facilitated the adsorption of pollutants and, hence, promoted the photocatalytic activity of the $ZnFe_2O_4$/rGO nanocomposite that was observed. In fact, the $ZnFe_2O_4$/rGO nanocomposite decomposed MB at a rate about 7.6 times higher than the pristine one [41].

3.2. Separation and Migration of Photoinduced Charge Carriers

Photogenerated electron–hole pair's recombination has been reported as one of the prime reasons for restricting the efficiency of photocatalysts. The recombination rate of an electron–hole pair is quite faster than their lifetime. Thus, they become recombined within a few nanoseconds of their production. This leads to the destruction of maximum charge carriers [42,43] The photocatalytic performance of MFs is greatly reduced owing to the rapid rate of recombination of charge carriers. The anchoring of GN sheets with MFs facilitates the mobility of photoinduced electrons, and, hence, the separation as well as transfer of excitons is improved significantly. This reduces the recombination rate and enables the excitons to be abundantly available at the photocatalyst's surface for carrying out redox reactions. As a result, the photocatalytic efficiency of MFGNs is improved considerably [44]. The enriched charge carriers' transfer and separation are assessed with the help of photoluminescence (PL), electrochemical impedance spectroscopy (EIS), and photovoltage–photocurrent response studies. Mokhtar et al. demonstrated the pronounced charge transfer and separation efficiency of a $MnFe_2O_4$/graphene composite using PL spectra at an excitation wavelength of 310 nm (Figure 3a). The maximum PL emission

intensity of pristine $MnFe_2O_4$ is at 460 nm, indicating a higher rate of recombination, whereas that of the $MnFe_2O_4$/graphene nanohybrid was much reduced. The diminished PL intensity is indicative of distinct electron and hole separation in the presence of graphene. The different coloured line in the PL spectra represents the emission efficiency of pristine $MnFe_2O_4$ along with its composite with graphene at different weight ratios [45]. The increased charge-separation efficiency of the prepared composite photocatalyst is due to the robust adherence of graphene with $MnFe_2O_4$. Electrochemical impedance spectroscopy (EIS) is useful to investigate the charge-transfer resistance in a semiconductor composite. Nazim et al. conducted EIS studies for $Co_xZn_{1-x}Fe_2O_4$ and its composite with rGO. From the EIS spectra given in Figure 3b, a large semicircle can be observed for pristine ferrite compared to that observed for the ferrite/rGO composite. This indicates a higher interfacial charge-transfer resistance in the case of pristine ferrite. Due to a lower resistance in the MFGN composite, the transfer of electrons to the graphene surface can conveniently occur. This process leads to boosted photocatalytic activity [46]. Fu et al. reported a conspicuous charge transfer and separation in $MnFe_2O_4$/graphene, with respect to that observed for pristine $MnFe_2O_4$ and GO. They observed that the photovoltage and photocurrent response of $MnFe_2O_4$/graphene is five times higher than that of $MnFe_2O_4$. For pristine $MnFe_2O_4$, the photocurrent of the electrode was reported to be 0.02 µA, whereas in the case of a $MnFe_2O_4$/graphene composite the value was increased to 0.098 µA. This indicates the prominent separation of the photogenerated electrons and holes in the composite as a result of the electronic interaction between the graphene sheets and MF [47].

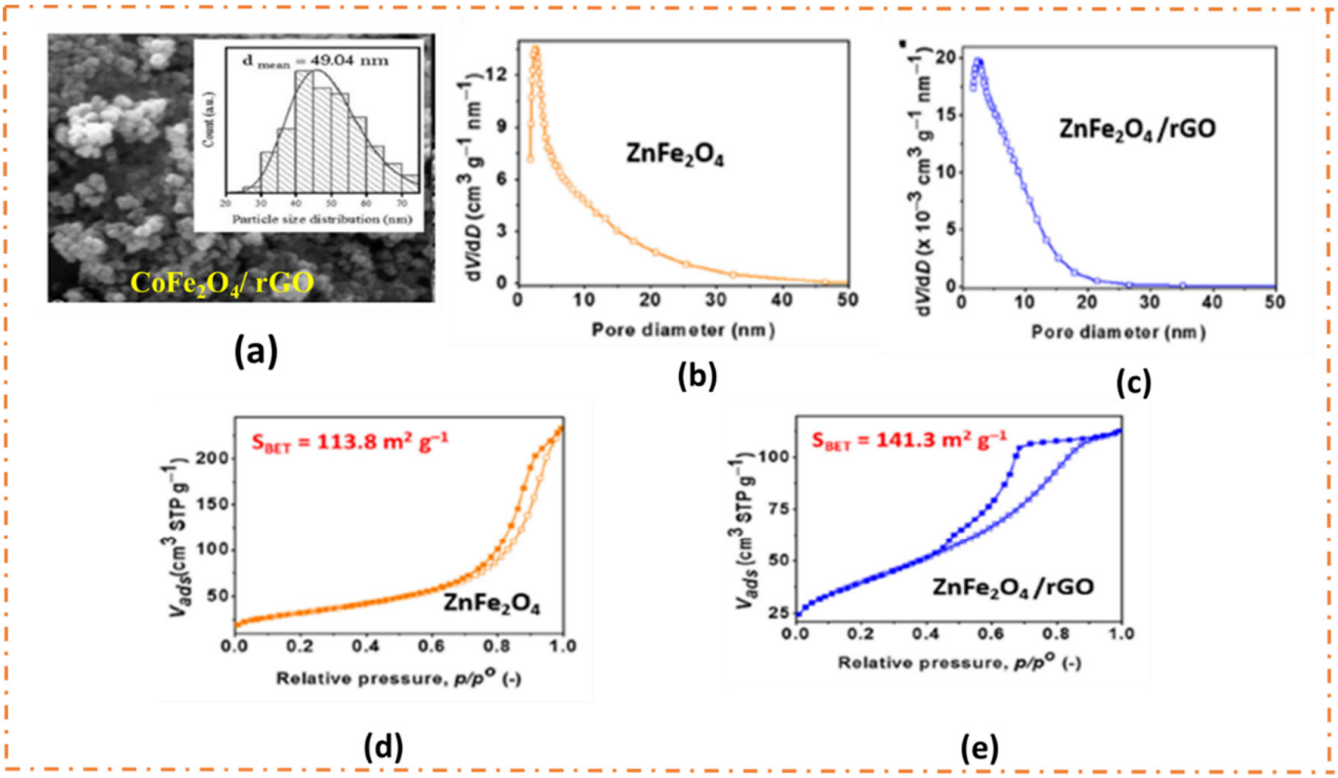

Figure 2. (**a**) FESEM image of $CoFe_2O_4$/rGO composite "Reprinted/adapted with permission from Ref. [40]. 2020, Elsevier". BJH adsorption pore size distribution curve for (**b**) $ZnFe_2O_4$ and (**c**) $ZnFe_2O_4$/rGO; N_2 adsorption–desorption isotherm for (**d**) $ZnFe_2O_4$ and (**e**) $ZnFe_2O_4$/rGO ("Reprinted/adapted with permission from Ref. [41]. 2020, Elsevier".

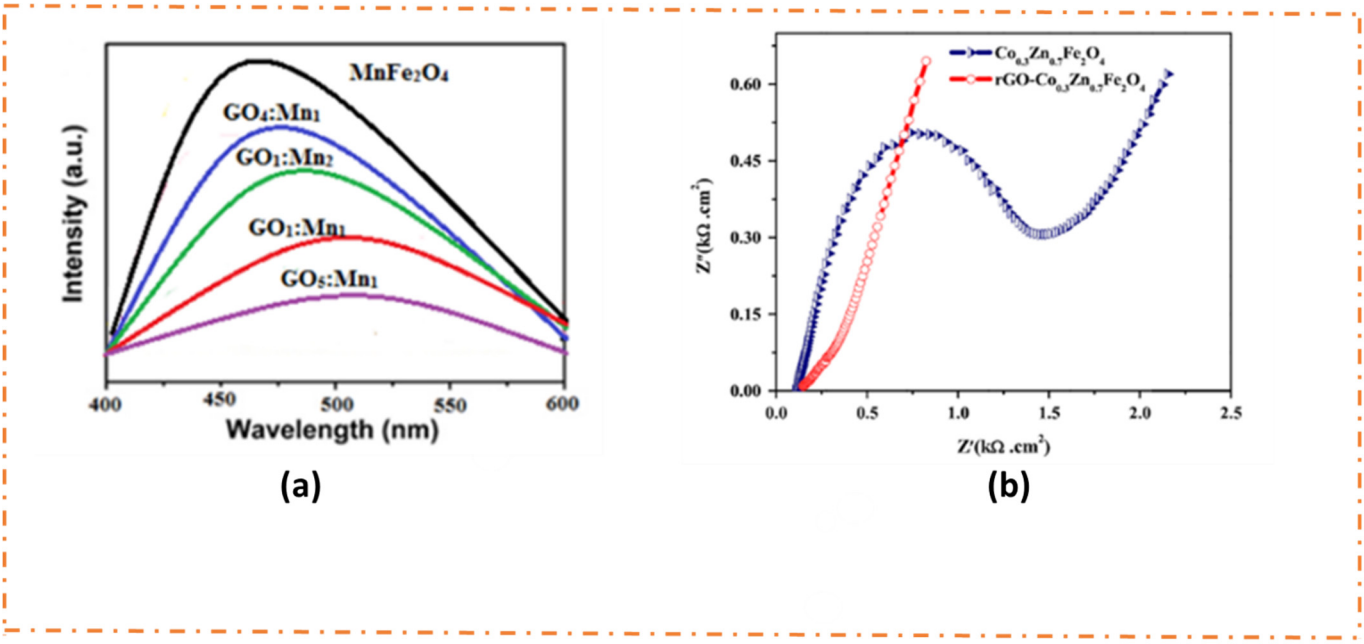

Figure 3. (**a**) PL spectra of $MnFe_2O_4$ and $MnFe_2O_4$/graphene composites (GO_4:Mn_1, GO_2:Mn_2, GO_1:Mn_1, and GO_5:Mn_1) "Reprinted/adapted with permission from Ref. [45]. 2016, Elsevier". (**b**) EIS spectra for $Co_xZn_{1-x}Fe_2O_4$ and $Co_xZn_{1-x}Fe_2O_4$/rGO "Reprinted/adapted with permission from Ref. [46]. 2016, Elsevier".

3.3. Light Absorption Range

The band gap energy of a semiconductor plays a crucial role in determining the photocatalytic activity. Although MFs with narrow band gap energies can harness visible light from solar radiation, the efficiency of absorption is poor owing to their contracted absorption window. To achieve significant activity, the MFs should be capable of absorbing visible light in a broad range, so the maximum amount of photon fluxes can be utilized [48]. This can be achieved with a red shift in the visible-light absorption of the MFs. Graphene and its analogues not only succor in charge trapping and migration but also facilitate the broadening of the visible-light-absorption range [49]. Therefore, coupling of graphene or its analogues with MFs shifts the light response to a longer wavelength along with a wider absorption range. This enables MFGN-composite photocatalysts to absorb and utilize solar radiation in a proficient way [50]. The Iqbal group prepared sheet-on-sheet nanocomposites such as $CaFe_2O_4$/graphene and studied the effects of the addition of graphene on light-absorption ability. The light-absorption range of pristine $CaFe_2O_4$ was extended to the visible region of a longer wavelength in the presence of graphene (Figure 4a). As evident from the Tauc plots shown in Figure 4b, the band gap energy (BGE) of the pristine MF decreases with the addition of graphene. The BGE for pristine $CaFe_2O_4$ was determined to be 1.93 eV, whereas that for a $CaFe_2O_4$/graphene (0.25) composite was found to be 1.91 eV. This decreasing trend in BGE is attributed to the strong interaction between the MF and GN. The XPS spectra of the prepared MFGN shows that the Ca 2p and Fe 2p peaks are shifted slightly toward the lower binding energy, indicating the formation of a Fe-O-C covalent bond. As a result, additional energy states are introduced between the conduction and valence band of $CaFe_2O_4$, and, thus, the BGE was decreased. The decreased BGE allows for a greater number of photons from the visible region to be absorbed. As a result, the $CaFe_2O_4$/graphene (0.25) exhibited superior visible-light-responsive photocatalytic performance and degraded 99.4% of the MB in 90 min [51]. The UV–visible diffusive reflectance spectra shown in Figure 4c represent the change in the light-absorption range of pristine $ZnFe_2O_4$ with the addition of graphene. It was observed that pure $ZnFe_2O_4$ had a strong peak around <625 nm in the visible region of the solar spectrum. Nevertheless,

with the introduction of graphene, the composite showed strong absorption peaks in the 650–800 nm range. The enhancement in the light-absorption range of pristine $ZnFe_2O_4$ was mainly caused due to the background absorption of rGO [52]. Liang et al. demonstrated that the visible-light response of a $NiFe_2O_4$/rGO composite was escalated by raising the rGO content from 0.2 to 0.35 g [53]. This could be attributed to the desired quantity of rGO, which reduces the reflection of visible light [24]. Therefore, MFGN with the required amount of GN exhibits pronounced photoactivity under visible-light illumination.

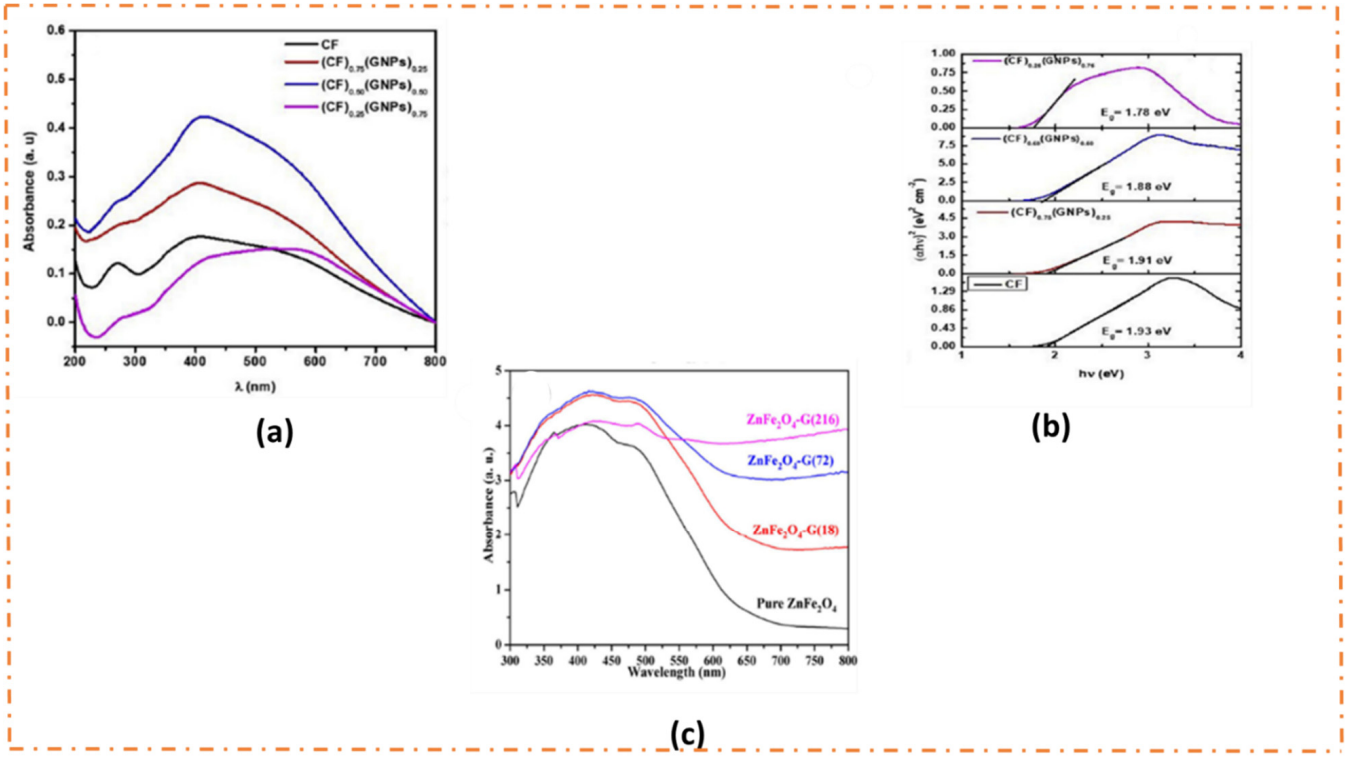

Figure 4. (**a**) UV–visible absorbance spectra and (**b**) Tauc plots for pristine $CaFe_2O_4$ and $CaFe_2O_4$/graphene composite with different amounts of graphene "Reprinted/adapted with permission from Ref. [51]. 2021, Elsevier". (**c**) UV–visible diffusive reflectance spectra of $ZnFe_2O_4$/rGO composite "Reprinted/adapted with permission from Ref. [52], 2020, Elsevier".

4. Fundamental Mechanisms for Photocatalytic-Dye Detoxification over MFGN

MFGN-based photocatalysis can be used as a breakthrough technology for the degradation of the organic dyes in aquatic systems. Photocatalytic organic dye detoxification takes place through a radical pathway, in which hydroxyl radical ($HO^{\bullet}$), holes (h^+) and superoxide ($O_2^{-\bullet}$) radicals are mainly involved. After the generation of electron–hole pairs from the MFs by the interaction of visible light of the suitable wavelength presented in Equation (1), the photoinduced electrons are conveniently transferred through the graphene sheet (Equation (2)), leading to the improved separation of electrons and holes [54].

$$\text{MFGN} + h\nu \rightarrow \text{MFGN}\ (h^+ + e^-) \quad (1)$$

$$e^- + \text{graphene} \rightarrow \text{graphene}\ (e^-) \quad (2)$$

The photoexcited and well-separated e^-s carry out reduction reactions with surface-adsorbed oxygen molecules to generate highly reactive superoxide (O_2^-) anions, as shown in Equation (3), only when the conduction band edge level of the MF lies above the potential of the O_2/O_2^- redox couple ($E^o_{O2/O2^{\bullet-}} = -0.33$V vs.NHE at pH 7.0). Similarly, strongly reactive ·OH radicals are produced through the water-oxidation reaction by the holes of the MFs with VB positions that are more positive than the redox potential of the

$H_2O/\cdot OH$ couple ($E^o_{H2O/\cdot OH} = 2.29$ V vs.NHE at pH 7.0) or that of the $OH^-/\cdot OH$ couple ($E^o_{OH-/\cdot OH} = 1.99$ V vs.NHE at pH 7.0), according to Equations (4) and (5) [55,56]:

$$O_2 + \text{graphene } (e^-) \rightarrow O_2{}^- \quad (3)$$

$$H_2O + h^+_{VB} \rightarrow \cdot OH + H^+ \quad (4)$$

$$OH^- + h^+_{VB} \rightarrow \cdot OH \quad (5)$$

Therefore, the Conduction Band (CB) and Valence Band (VB) positions of the MFs play a pivotal role in determining the mechanistic pathways for the photodecomposition of organic dyes. Based on the potential band edge values, MFs can be classified into three categories, as presented in Scheme 2. These are (i) MFs with a strong reduction ability, (ii) MFs with a strong oxidation ability, and (iii) MFs with a moderate redox ability. Depending on the redox abilities of the MFs, the photodetoxification of dye molecules over the MFGNs proceeds by following three different routes.

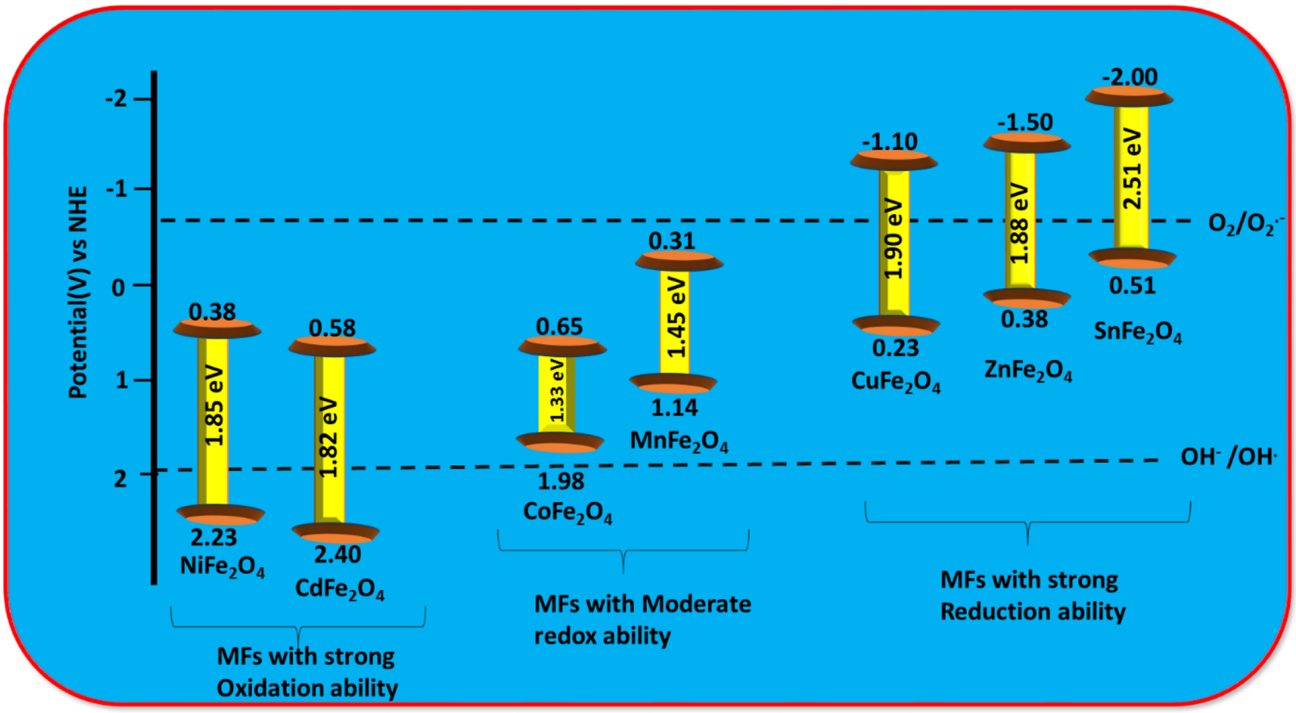

Scheme 2. The classifications of MFs based on their redox abilities and their band edge potentials.

4.1. Mechanism for Photodetoxification of Dyes over MFGNs with Strong Reduction Ability

The photoinduced electrons of MFGNs with a strong reduction ability, owing to the more negative CB levels of MFs such as $ZnFe_2O_4$, $SnFe_2O_4$, etc., are comfortably transported to the surface of graphene or its derivatives. These electrons reduce the surface-adsorbed O_2 molecules to $O_2{}^-$ species, which decomposes the dye molecules according to Equation (6). On the other hand, the photogenerated holes at the VB of the MFs with an adequate potential can take part in the process of

$$O_2{}^- + \text{Dye} \rightarrow CO_2 + H_2O \quad (6)$$

$$\text{MFGN } (h^+) + \text{Dye} \rightarrow \text{Degraded products} \quad (7)$$

dye detoxification, per Equation (7). However, the possibility of the formation of ·OH radicals through the holes-driven water-oxidation reaction is overruled due to the inadequate VB levels of these MFs. However, the production of ·OH radicals was ascertained with

the help of the photo-Fenton reaction mechanism. According to this, the photogenerated electrons on the graphene sheets reduce H_2O_2 into ·OH and OH^-, per Equation (8) [57].

$$\text{Graphene } (e^-) + H_2O_2 \rightarrow OH^{\cdot} + OH^- + \text{Graphene} \quad (8)$$

$$Fe^{3+} + OH^- \xrightarrow{h\nu} Fe^{2+} + OH^{\cdot} \quad (9)$$

Then, the Fe^{3+} ions of MFGN combine with OH^- ions in the presence of light energy to form Fe^{2+} ions and ·OH radicals (Equation (9)). Similarly, the M^{2+} ions of MFGN undergo a reaction with H_2O_2 to liberate ·OH radicals and form M^{3+} ions, according to Equation (10). The Fe^{2+} ions that are formed are oxidized by H_2O_2, as presented in Equation (11), to produce Fe^{3+} ions as well as ·OH radicals. Additionally, these ions also convert M^{3+} ions into M^{2+} ions, as presented in Equation (12). The strongly reactive ·OH radicals that are formed participate in dye degradation, per Equation (13) [58,59]

$$M^{2+} + H_2O_2 \rightarrow M^{3+} + OH^- + OH \quad (10)$$

$$Fe^{2+} + H_2O_2 \rightarrow Fe^{3+} + OH^- + OH \quad (11)$$

$$Fe^{2+} + M^{3+} \rightarrow Fe^{3+} + M^{2+} \quad (12)$$

$$OH^{\cdot} + \text{Dye} \rightarrow H_2O + CO_2 \quad (13)$$

The overall photodegradation process is presented in Scheme 3. Baynosa et al. reported that the photon-produced electrons at the CB of $ZnFe_2O_4$ migrate to the rGO surface, where they reduce the adsorbed O_2 to form O_2^-. The obtained O_2^- species undergo degradation of MB. Concurrently, the holes produced at the VB of $ZnFe_2O_4$ directly decompose MB molecules without producing HO• radicals, as the VB level of $ZnFe_2O_4$ is placed above that of the H_2O/·OH couple. They carried out scavenging tests in order to provide evidence in support of the existence of O_2^- and h^+ as the primary reactive species. Figure 5a shows that the decrease in photodegradation was found to be 70.8%, 23.2%, and 4.6% in the presence of p-benzoquinone (pBQ), $NaHCO_3$, and isopropyl alcohol (IPA), respectively, which are the quenchers for O_2^-, h^+, and HO•, respectively. These experimental pieces of evidence suggest that O_2^- and h^+ are the primary reactive species for the photodegradation of MB by a $ZnFe_2O_4$/rGO composite [41]. In a similar investigation, the Qu group demonstrated that O_2^- and h^+ are the prime reactive species for the photodegradation of AO7 over $CuFe_2O_4$/GO composites. The possibility of the formation of HO• radicals is ruled out, since the VB position of $CuFe_2O_4$ is more anodic than that required to undergo WOR. On the other hand, the more negative CB level of $CuFe_2O_4$ enables the photoinduced electrons to reduce O_2 molecules into O_2^- species [60]. However, Lu et al. demonstrated that the major reactive species is the HO• radicals, which are produced by the photoelectrochemical decomposition of H_2O_2 over the $ZnFe_2O_4$/graphene surface with the help of photon-generated electrons, according to Equation (8). In order to ascertain the formation of the HO• radicals, Lu et al. carried out fluorescent spectral studies using fluorescent probe terephthalic acid (TA). Upon the interaction of visible light, TA easily reacted with the OH· radicals to form highly fluorescent 2-hydroxy terephthalic acid (TAOH), with fluorescent spectral peak intensities at 430 nm (Figure 5b) that increased with an increase in time span. This evidences that under visible-light illumination and in the presence of H_2O_2, a $ZnFe_2O_4$/graphene composite produces OH· radicals, which play a vital role in the degradation of organic dyes [61]. The h^+s are reported as the major active species for the photocatalytic Congo red degradation on the $ZnFe_2O_4$/graphene composite, as only 6.9% of the dye was degraded in the presence of EDTA, which acts as the h^+ scavenger. In addition, the OH· radicals and O_2^- species are also involved in the degradation process [62]. In another study, Fan and co-authors suggested that the dye decomposition reaction over the $ZnFe_2O_4$/graphene composite might involve the Fenton and photo-Fenton processes, as presented in Equations (8)–(13) [24].

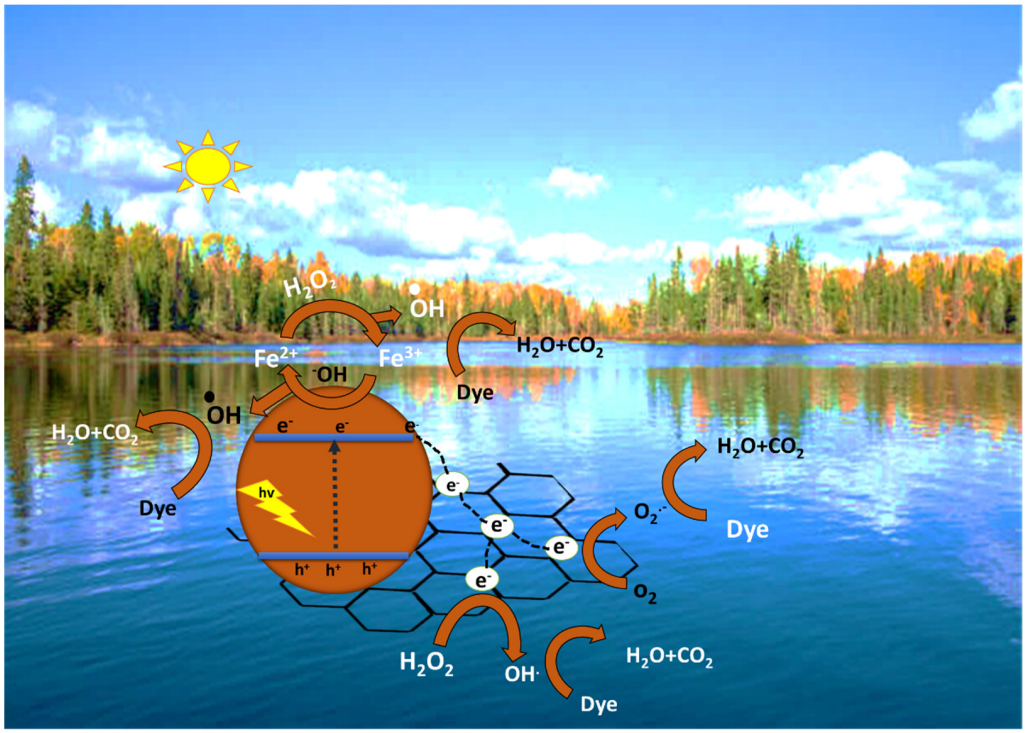

Scheme 3. Schematic representation for mechanism of dyes' photodetoxification by MFGNs with strong reduction ability.

4.2. Mechanism for Photodetoxification of Dyes over MFGNs with Strong Oxidation Ability

The VB positions of MFs such as $NiFe_2O_4$, $CdFe_2O_4$, etc., are relatively more cathodic than the potential needed for water oxidation, as presented in Scheme 2. Therefore, the holes at the VB of MFs acquire strong oxidation abilities to convert H_2O/OH^- into strongly reactive OH· species, which acts as a strong oxidant for the mineralization of the dyes. Further, the photogenerated electrons are migrated to the graphene surface and reduce the O_2 molecules into O_2^- species, which also takes part in the photodegradation process. Moreover, the holes at the VB of MFs receive enough potential to degrade the dyes. The detailed process for photocatalytic-dye degradation is explained in Scheme 4. According to the Chen group, the photogenerated electrons from the CB of $NiFe_2O_4$ are conveniently transferred to an RGO sheet due, to its excellent electron-transport property. This substantially improved the separation efficiency of the excitons. The electrons reduce the O_2 molecules into O_2^- anions at the RGO surface. In the meantime, the holes at the VB of $NiFe_2O_4$ with a robust oxidation ability react with OH^- ions to form OH· radicals. In addition, a portion of the holes directly react the dye molecules into harmless products. Generally speaking, h^+, ·OH, and O_2^- are involved in the efficient photodegradation of MB [53]. Mandhakini and co-authors proposed the decreasing tendency of different reactive species for the degradation of MB over $NiFe_2O_4$/rGO composites as ·OH > O_2^- > h^+ > e^- [63]. A similar observation was reported by Rahman et al. for the photodecomposition of MB with the help of Ce-substituted $NiFe_2O_4$/rGO. However, the role of electrons in the dye-degradation process is considered negligible [64].

4.3. Mechanism for Photodegradation of Dyes over MFGNs with Moderate Redox Ability

Spinel ferrites such as $CoFe_2O_4$, $MnFe_2O_4$, etc., experience a moderate redox ability, as their VB and CB positions are placed above the potential required for water oxidation and below the potential needed for O_2 reduction, respectively. Since the direct production of ·OH and O_2^- from WOR and ORR, respectively, is thermodynamically unreasonable, the dye-degradation pathway proceeds through the photo-Fenton mechanism that was depicted in Section 4.1 and presented in Equations (8)–(13). Wei and co-authors demonstrated

that $MnFe_2O_4$/rGO nanocomposites degraded MB efficiently through the photo-Fenton process [65]. In another set of experiments, ·OH radicals were found as the primary reactive species in the photodecolorization of MO and MB over $CoFe_2O_4$/rGO composites, and these were generated through the photo-Fenton mechanism [66]. Mazarji et al. conducted scavenging experiments in order to confirm the major reactive species that takes part in the degradation of BR46 over rGO-$CoFe_2O_4$ by the photo-Fenton process. They used ethanol, DMSO, and EDTA as scavenging agents for $OH^{\cdot}$, O_2^-, and h^+, respectively. Figure 5c shows that the dye-degradation reaction was significantly suppressed in the presence of ethanol, suggesting that ·OH played the principal role in the pollutant degradation [67].

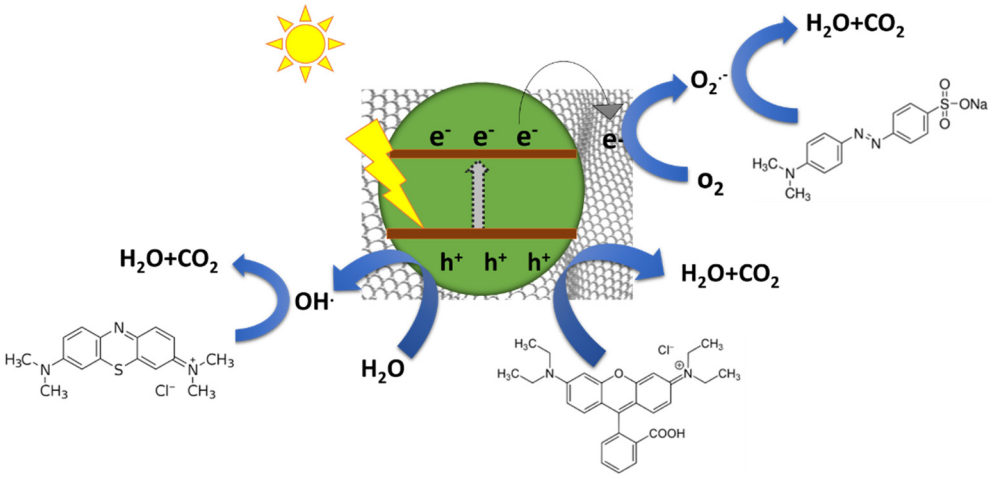

Scheme 4. Mechanism for photodegradation of dyes over MFGNs with strong oxidation ability.

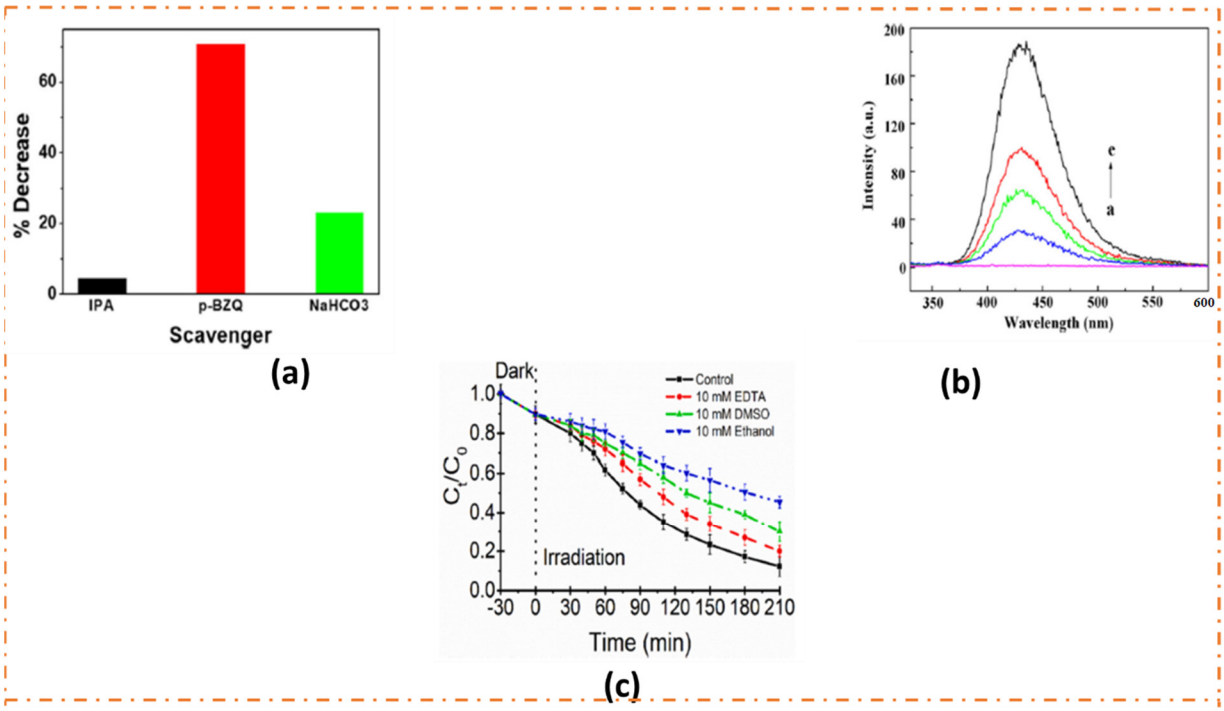

Figure 5. (**a**) Scavenging tests for MB photodegradation by $ZnFe_2O_4$/rGO "Reprinted/adapted with permission from Ref. [41]. 2020, Elsevier" (**b**) fluorescent spectra of 2-hydroxy terephthalic acid (TAOH) for dye degradation over $ZnFe_2O_4$/graphene surface after (a) 0, (b) 1,(c) 3, (d) 5, and (e) 10 min, respectively "Reprinted/adapted with permission from Ref. [61]. 2013, Elsevier". (**c**) degradation rate of BR46 dye over rGO-$CoFe_2O_4$ in presence of different quenching reagents "Reprinted/adapted with permission from Ref. [67]. 2021, Elsevier".

The major disadvantage of the photo-Fenton process is that it is usually carried out at a pH less than 3.0, as Fe^{3+} becomes precipitated as $Fe(OH)_3$ at higher pH values [68]. Further, the SO_4^- species generated from peroxymonosulfate (PMS) activation is considered as a potential candidate for the degradation of dyes [69]. The mechanism of dye detoxification through PMS activation is as follows. The metal ions (M^{2+}) of MFGN, in the presence of catalytically activated PMS, produce SO_4^- and M^{3+}, as shown in Equation (14). The M^{3+} and Fe^{3+} ions undergo reduction by MFGN-activated PMS (Equations (15) and (16)) to M^{2+} and Fe^{2+}, respectively. The oxidation of Fe^{2+} ions in the presence of PMS, per Equation (17), led to the regeneration of Fe^{3+} along with the formation of SO_4^-. The release of SO_4^- can also occur by the reaction of PMS with electrons provided by rGO, per Equation (18). The SO_4^- species that is formed is strongly reactive and decomposes the organic dyes efficiently into harmless products, as shown in Equation (19) [70].

$$HSO_5^- + M^{2+} \rightarrow M^{3+} + SO_4^- + OH^- \quad (14)$$

$$HSO_5^- + M^{3+} \rightarrow M^{2+} + SO_5^- + H^+ \quad (15)$$

$$HSO_5^- + Fe^{3+} \rightarrow Fe^{2+} + SO_5^- + H^+ \quad (16)$$

$$HSO_5^- + Fe^{2+} \rightarrow Fe^{3+} + SO_4^- + OH^- \quad (17)$$

$$HSO_5^- + e_{CB}^- \rightarrow SO_4^- + OH^- \quad (18)$$

$$Dyes + SO_4^- \rightarrow H_2O + CO_2 \quad (19)$$

The Qi group used $CoFe_2O_4$/rGO to degrade organic contaminants such as Carbamazepine (CBZ), Tetracycline (TC), Rhodamine B (RhB), and Congo Red (CR) through PMS activation under LED illumination. They observed a complete degradation of dyes (RhB and CR) within 10 min [71].

5. Reaction Kinetics for Photocatalytic-Dye Degradation over MFGN

Kinetic study is an important strategy to evaluate the performance of a photocatalyst. The photocatalytic degradation of dyes follows the pseudo-first-order rate equation, per the Langmuir–Hinshelwood model [72]. This model can be expressed by Equation (20).

$$ln\frac{C_0}{C_t} = kt \quad (20)$$

where C_0 represents the initial dye concentration, C_t is the concentration at any time t under solar light, and k is the rate constant. The value of the rate constant is graphically calculated from the slope of the straight line obtained by plotting the values of $ln\frac{C_0}{C_t}$ vs. time (t). Zhang and co-workers reported that the k value for MB degradation over pristine $CdFe_2O_4$ was increased by 5 times, from 0.00145 to 0.00543 min^{-1}, upon the integration of graphene. This impressive increase in the k value for the $CdFe_2O_4$/graphene nanocomposites suggested their superior performance over the pristine one [73]. Higher rate constant values were also observed for $MnFe_2O_4$/rGO (0.019 min^{-1}) in contrast to bare $MnFe_2O_4$ (0.012 min^{-1}) during PMS-activated Orange II degradation. The composite photocatalyst exhibited a high rate of photodegradation of Orange II in the presence of anions such as Cl^-, HCO_3^-, NO_3^-, and CH_3COO^-, which are commonly available in waste water. The degradation rate was observed in the order: $NO_3^- < CH_3COO^- < HCO_3^- < Cl^-$ [74]. The Zou group also separately studied the effect of Cl^- concentration on the degradation of diclofenac and acetaminophen [75–78]. The degradation rate constant for Orange II was increased from 0.019 to 0.156 min^{-1} with an increase in the Cl^- concentration from 0 to 0.1 M. The Cl^- ions are oxidized to reactive chlorine species such as Cl_2 and HOCl at a higher Cl^- concentration, per Equations (21) and (22), respectively. These active chlorine species undergo degradation of Orange II, thereby increasing the degradation rate constant [74].

$$2Cl^- + HSO_5^- + H^+ \rightarrow SO_4^{2-} + Cl_2 + H_2O \quad (21)$$

$$Cl^- + HSO_5^- \rightarrow SO_4^{2-} + HOCl \quad (22)$$

the $MnFe_2O_4$/rGO composite also exhibited an excellent degradation efficiency for the decomposition of methyl violet (MV), MO, MB, and Rhodamine B (RhB) including Orange II [74]. In general, MFGN photocatalysts can be considered as proficient photocatalysts for organic dye degradation.

6. Impact of Reaction Parameters on Photocatalytic-Dye Detoxification by MFGNs

Reaction parameters such as solution pH, catalyst dose, dye concentration, and temperature significantly influence the dye-degradation performance of the photocatalysts [79]. Studies optimized these parameters for the maximum efficiency of MFGNs for the photodetoxification of dyes.

6.1. pH of the Solution

The greater the extent of adsorption of the dye molecules on the MFGN surface, higher is the maximum photodegradation efficiency. Dye adsorption is largely influenced by the nature of the dye and the surface charge that appears on MFGN [80]. The pH of the dye solution strongly influences the surface charge of MFGN and, hence, the extent of dye adsorption. The photocatalytic activity of the $NiFe_2O_4$/GO nanocomposites were compared at different pH conditions. At a low pH, the surface of the composite photocatalyst becomes positively charged (as $pH < pH_{pzc}$). Since MB is a cationic dye, it occupies positive charges, which are repelled from the catalyst surface, acquiring similar charges. As a result, MB molecules could not effectively be adsorbed on the photocatalyst, and a dismal photocatalytic detoxification performance was observed. Conversely, $NiFe_2O_4$/GO surfaces attain negative charges under alkaline conditions where $pH > pH_{pzc}$. This expedites the positively charged MB molecules to become greatly adsorbed on the negatively charged composite surfaces through electrostatic attraction, and the composite photocatalyst exhibited impressive performance for MB degradation. Additionally, the diffusion of surface-generated hydroxyl radicals resulted in the maximum degradation of MB at a higher pH. The composite showed its maximum MB degradation of 90.84% at pH 10 [81]. Zhang et al. also reported similar results for the degradation of MB over a $CdFe_2O_4$/graphene composite. They achieved more than 94% MB degradation at pH 9–10 [73].

6.2. Temperature

The degradation of organic dye over a photocatalyst is largely influenced by temperature. The collision probability between the dye and the photocatalyst increases with an increase in temperature. This leads to an enhanced photodegradation efficiency, and maximum dye decomposition is observed at a particular temperature [82]. A further increase in temperature causes the desorption of dye molecules from the photocatalyst surface. As a result, the photodegradation rate is substantially decreased. Liang and co-workers studied the effect of temperature on photocatalytic MB degradation over a $NiFe_2O_4$/rGO composite. The degradation rate constant (k) started increasing with an increase in temperature up to 25 °C. However, the rate constant value was significantly decreased by raising the temperature further (Figure 6a) [53]. Therefore, 25 °C is considered as the optimum temperature for maximum photodetoxification.

6.3. Catalyst Dosage

Catalyst dosage/loading indicates the minimum amount of MFGN photocatalyst required for the maximum photodegradation of a dye. It has a distinct role in photocatalytic-dye detoxification. Kodasama et al. studied the effect of $CuFe_2O_4$/GO loading on the photocatalytic decomposition of reactive black 5 (RB5). They observed that the degradation of RB5 was increased from 66.7% to 100%, when the catalyst dose was raised from 0.05 g/L to 0.5 g/L. This could be attributed to the increase in the number of active sites and the surface area of the composite photocatalyst, when increasing the catalyst dose's amount. The availability of an enlarged surface area and a higher number of surface active sites

facilitated the adsorption of dye molecules on $CuFe_2O_4$/GO. Moreover, an increase in the mass-to-volume ratio of the photocatalyst accelerated the light-absorption efficiency. As a result, an improved photodegradation performance was observed [83]. Yuan and co-authors demonstrated, as shown in Figure 6b, that 50 mg (0.5 g/L) of $ZnFe_2O_4$/rGO displayed the maximum MB degradation. A further increase in the catalyst amount led to a decrease in the photodetoxification, probably due to the blockage of active sites that resulted from the increased extent of agglomeration [84]. In addition, the increased agglomeration prevented the passage of visible light, due to which the dye-degradation rate is decelerated.

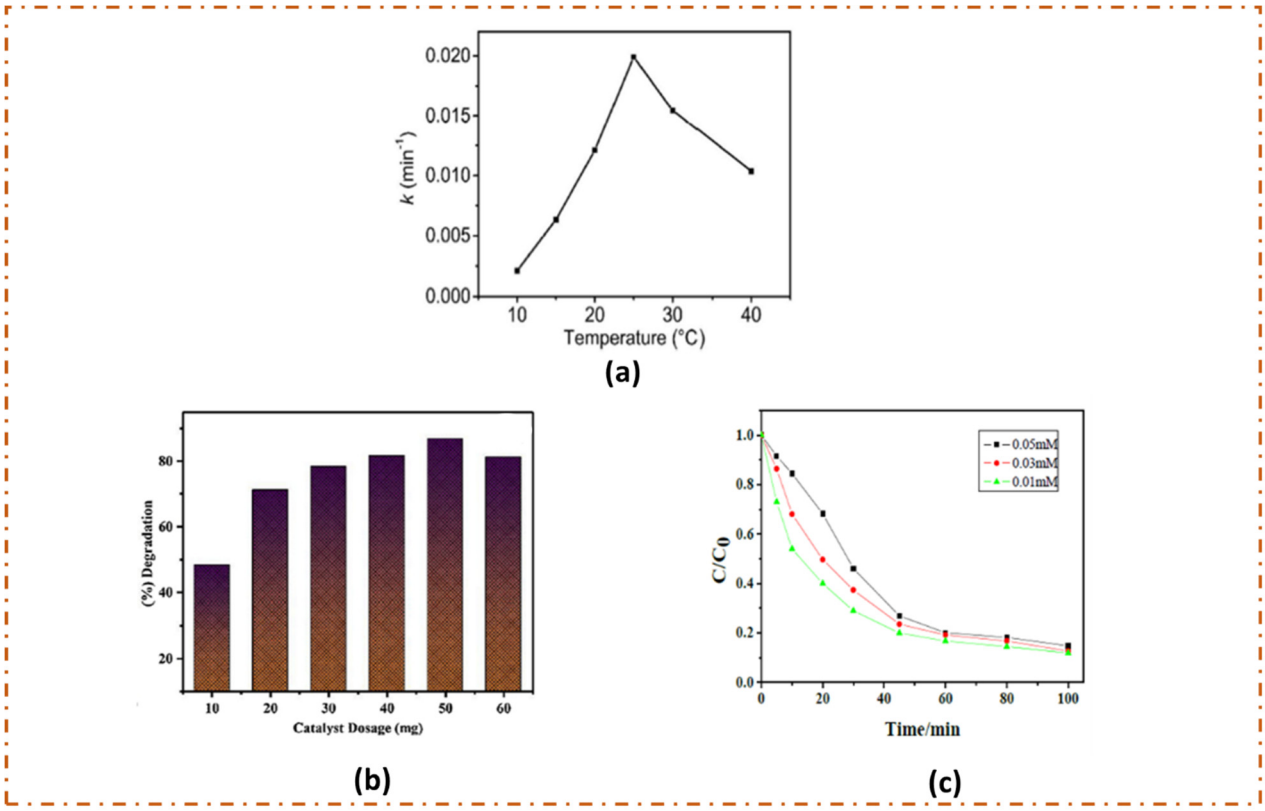

Figure 6. (**a**) Effect of temperature on MB degradation rate "Reprinted/adapted with permission from Ref. [53]. 2018, ACS". (**b**) Effect of $ZnFe_2O_4$/rGO catalyst dosage on MB degradation "Reprinted/adapted with permission from Ref. [84]. 2021, Elsevier" (**c**) effect of initial AO7 concentration on its degradation over $CuFe_2O_4$/GO surface "Reprinted/adapted with permission from Ref. [60]. 2016, Elsevier".

6.4. Effect of Dye Concentration

The initial dye concentration has a major role in the photocatalytic-dye-degradation process. With an increase in dye concentration, the active sites on the surface of the MFs are accommodated by the dye molecules and gradually attain saturation. Therefore, the light-absorption efficiency of the photocatalyst is largely affected [85,86]. This caused the inadequate production of photogenerated charge carriers, due to which the photodetoxification efficiency of the MFGNs was greatly lowered. Chen et al. investigated the effect of initial AO7 concentration on its degradation over a $CuFe_2O_4$/GO surface. They observed that the rate of photodegradation for AO7 was decreased with an increase in its concentration (Figure 6c) [60]. However, Shang and co-authors demonstrated that a $CoFe_2O_4$/graphene composite took 2 h for the complete decomposition of a 20 $mg{\cdot}L^{-1}$ MB solution, while a 40 $mg{\cdot}L^{-1}$ MB solution was completely degraded in 3 h. Dye degradation initially takes place slowly at a higher concentration due to the diminished light-absorption capacity. After the degradation of some of the dyes, the light response was improved,

which enhanced the degradation rate and complete degradation occurs at longer time span [87].

7. Comparison of Photocatalytic Performance of MFGNs for Dye Detoxification

MFGNs exhibited excellent performance for the photocatalytic degradation of organic dyes with respect to that of pristine MFs. The performances of various MFGNs were compared with those of bare MFs and are listed in Table 1. Mandal et al. reported that 97% of MB was degraded within 60 min over a $MnFe_2O_4$/rGO composite, whereas bare $MnFe_2O_4$ nanoparticles degraded only ~84% in 290 min [88]. Mokhtar et al. also demonstrated that a $MnFe_2O_4$/graphene oxide composite degraded 100% of MB in 60 min. The degradation efficiency was found to be four times better than that displayed by its pristine counterpart [45]. These results suggest that the incorporation of graphene into MFs facilitated the transport of photoinduced electrons through its large aromatic structure, and, hence, the recombination of the electron–hole pairs was appreciably hindered. This led to an improved photocatalytic performance. Gan et al. fabricated $CoFe_2O_4$/graphene composites containing 5, 10, 20, and 40 wt % of graphene and compared their photocatalytic performance for MB degradation. Only ~34% of MB was degraded by pristine $CoFe_2O_4$ in 2 h. Conversely, the $CoFe_2O_4$/graphene nanocomposites exhibited a much higher efficiency for dye degradation. The $CoFe_2O_4$/graphene (5 wt%) required 2 h to degrade 100% of the MB present in the system. When the graphene content was increased to 10 wt%, the photocatalytic activity increased further. In particular, the photocatalyst required only about 1 h to complete the degradation process. However, the photocatalytic activity was adversely affected with a further increase in graphene content. Complete MB degradation was observed after 2 and 3 h, when the composite photocatalyst contained 20 and 40 wt% of graphene, respectively. It was confirmed that 10 wt% of graphene was the adequate amount to form a robust interaction with $CoFe_2O_4$, due to which the composite exhibited its maximum degradation efficiency. A further increase in the graphene content blocked the surface active sites of $CoFe_2O_4$ for the dye molecules, and, hence, the degradation efficiency was considerably decreased [87].

Table 1. Comparison in performance of MFGNs for photocatalytic-dye detoxification with pristine MFs.

SFGNs	Targeted Dye	Catalyst Dosage (gL^{-1})	Initial Dye Conc. (mgL^{-1})	Degradation Efficiency (%)	Number of Times Increase in Activity w.r.t. Pristine SF	References
$CoFe_2O_4$/rGO	BR46	0.02	20	62	1.45	[67]
$CoFe_2O_4$/rGO	BR18	0.02	20	79	2.25	[67]
$ZnFe_2O_4$/rGO	MB	0.5	10	98.0	7.6	[41]
$MnFe_2O_4$/GO	MB	0.3	10	97	1.15	[89]
$MnFe_2O_4$/GO	MB	0.25	20	100	1.2	[47]
$CaFe_2O_4$/G	MB	0.2	10	99.4	1.7	[51]
$CdFe_2O_4$/G	MB	1	10	89.22	2.2	[73]
$CoFe_2O_4$/GO	MB	0.25	10	~100	2.9	[87]
$ZnFe_2O_4$/G	Congo red	0.5	15	92.21	2.3	[62]
$MnFe_2O_4$/rGO	Orange II	0.05	20	90	1.6	[74]
Ce-doped $NiFe_2O_4$/rGO	MB	0.1	10	94.67	1.8	[64]
$ZnFe_2O_4$/G	RhB	1	20	100	3.3	[61]
$ZnFe_2O_4$/rGO	MB	0.5	50	92.4	1.04	[84]
$MnFe_2O_4$/rGO	MB	0.4	-	62	1.7	[65]

Table 1. *Cont.*

SFGNs	Targeted Dye	Catalyst Dosage (gL^{-1})	Initial Dye Conc. (mgL^{-1})	Degradation Efficiency (%)	Number of Times Increase in Activity w.r.t. Pristine SF	References
$MnFe_2O_4$/GO	MB	1	10	100	4	[45]
$ZnFe_2O_4$/G	MB	0.2	50	84	1.7	[24]
$CoFe_2O_4$/rGO	MB	0.5	5	74	~1.4	[40]
$NiFe_2O_4$/rGO	MB	0.25	20	99.1	~90	[53]
$CoFe_2O_4$/rGO	MB	0.25	20	100	-	[36]
$CoFe_2O_4$/rGO	RhB	0.25	20	72.2	-	[36]
$CoFe_2O_4$/rGO	MO	0.25	20	37.5	-	[36]
$CoFe_2O_4$/G	MB	0.25	20	100	~10	[72]
$CoFe_2O_4$/G	RhB	0.25	20	94	-	[72]
$CoFe_2O_4$/G	MO	0.25	20	71	-	[72]
$CoFe_2O_4$/G	Active-black BL-G	0.25	20	66	-	[72]
$CoFe_2O_4$/G	Active-red RGB	0.25	20	61	-	[72]
$CoFe_2O_4$/rGO	MB	1	10	73	~20	[32]
$CoFe_2O_4$/rGO	MO	0.5	20	100	-	[54]
$CoFe_2O_4$/rGO	MB	0.5	30	100	-	[54]
$CoFe_2O_4$/rGO	RhB	0.5	25	100	-	[54]
$CoFe_2O_4$/rGO	RhB	0.2	10	~100	~4	[71]
$NiFe_2O_4$/rGO	MG	0.2	-	96.5	~1.5	[63]
$ZnFe_2O_4$/Graphene	MO	1	15	5	-	[52]
$ZnFe_2O_4$/Graphene	MB	1	15	56	-	[52]
$ZnFe_2O_4$/Graphene	RhB	1	15	15	-	[52]
$NiFe_2O_4$/GO	MB	0.5	-	~40	-	[81]

8. Stability and Recoverability

The stability of a photocatalytic system under operating conditions is a vital aspect for its practical applications. Photocatalysts with substantial chemical and physical stability can be recovered and reused frequently. This increases their cost-effectiveness and makes them decorous for large-scale production [20]. The presence of graphene in MFGNs acts as a support material, and spinel ferrite nanoparticles are decorated over graphene surface through strong chemical bonds. This anchorage enables MFGNs to be used frequently without any noticeable loss in physicochemical properties. The magnetically recoverable rGO/$ZnFe_2O_4$ nanocomposite showed no significant decrease in its photocatalytic activity regarding MB detoxification for up to nine consecutive cycles, and the degradation rate was maintained above 90% for each cycle [88]. Rahman and co-workers reported that a Ce-doped Nickel ferrite/rGO composite retained its crystal structure even after five consecutive cycles. They observed no such significant change in the XRD pattern of the sample after being used for five runs (Figure 7a). Any changes in the chemical bonding and structure after reuse can easily be evident from FTIR studies. Figure 7b shows the FTIR data for a Ce-doped $NiFe_2O_4$/rGO composite before and after use. It was observed from the spectra that the vibrational modes are quite similar for both the samples, except for some disturbances in the peaks around 1250 and 1000 cm^{-1} for the fresh sample. The deviation might be due to the presence of MB. This suggests that the MB was completely mineralized over the photocatalyst under visible-light irradiation [64]. Yin et al. studied the microstructural changes in a $CoFe_2O_4$/rGO nanocomposite after six consecutive cycles.

They compared the TEM image of the prepared nanocomposite with that obtained after six cycles of dye degradation (Figure 7c). The two images showed no remarkable changes, revealing that the composite photocatalyst retained its morphology even after six cycles of use, and the ferrite nanoparticles were arranged uniformly as before on the exfoliated graphene sheets [31]. These reported pieces of evidence prove the extraordinary stability exhibited by MFGN nanocomposites for the photodetoxification of organic dyes.

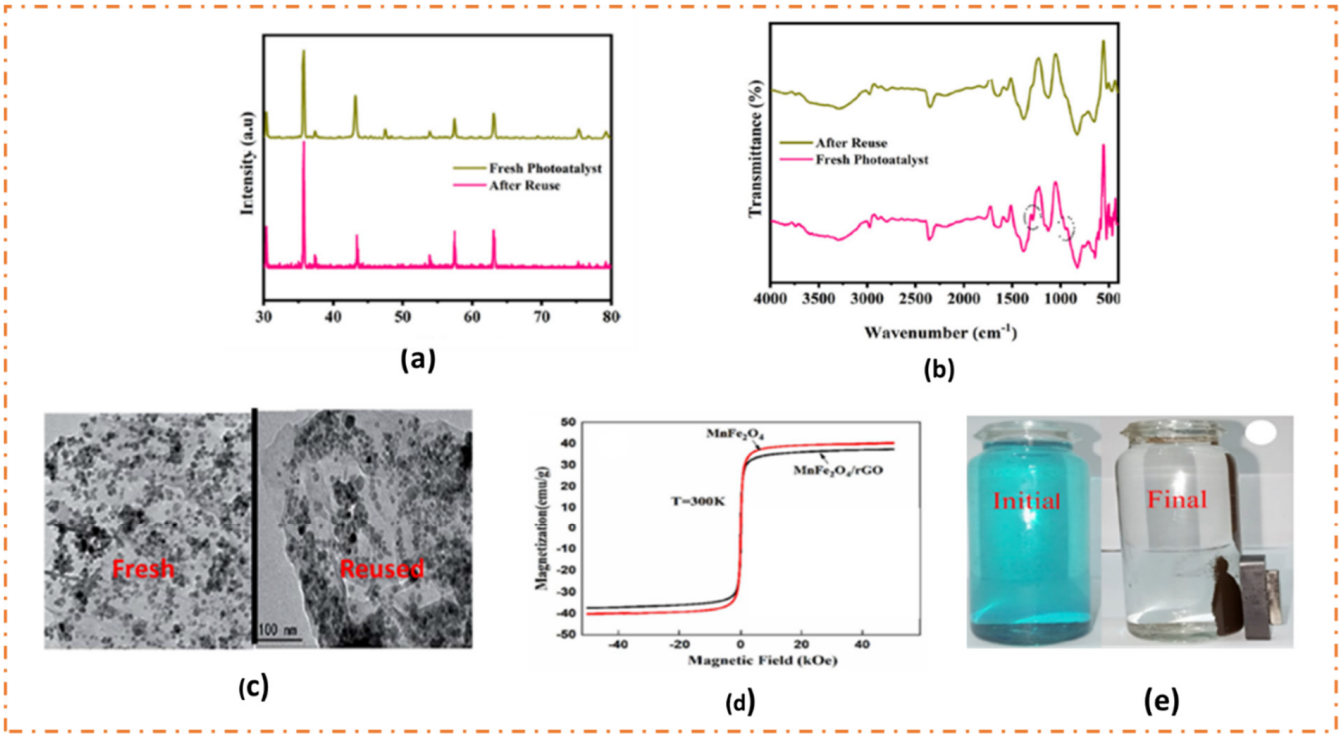

Figure 7. (**a**) XRD and (**b**) FTIR peaks of Ce-doped Nickel ferrite/rGO before and after reuse "Reprinted/adapted with permission from Ref. [64]. 2020, Elsevier". (**c**) TEM images of fresh $CoFe_2O_4$/rGO before and after 6th generation of use "Reprinted/adapted with permission from Ref. [31]. 2017, RSC". (**d**) Magnetic hysteresis of $MnFe_2O_4$ and $MnFe_2O_4$/rGO composite "Reprinted/adapted with permission from Ref. [89]. 2019, Elsevier". (**e**) Recovery of nickel ferrite/rGO composite from dye-degradation system using a magnet "Reprinted/adapted with permission from Ref. [90]. 2020, Elsevier".

The facile recoverability of a photocatalyst from a treated solution is another important criterion for large-scale application. MFGNs contain MFs as magnetic components, which can conveniently be separated from the suspension with the help of an external magnetic field. Mandal et al. studied the magnetic hysteresis of $MnFe_2O_4$ and a $MnFe_2O_4$/rGO composite using a vibrating sample magnetometer (VSM). They found that both of them show a super-magnetic nature. The saturation magnetization of bare ferrite was found to be 41 emu g^{-1}. However, Mandal et al. observed that the magnetic behavior of the $MnFe_2O_4$/rGO nanocomposite is weakened to a small extent with a saturation magnetization of 37 emu g^{-1} (Figure 7d). As graphene is a magnetically inactive material, it reduces the saturation magnetization value of the composite photocatalyst [89]. Nevertheless, the composite can still be magnetically separated from the applied solution. Figure 7e shows the facile recovery of a $NiFe_2O_4$/rGO composite from a dye-degradation system using an external magnetic field [90].

9. Conclusions

Dye-containing effluents contribute significantly to elevating the level of water pollution. Among existing techniques, the semiconductor-mediated photocatalytic detoxification

of dyes is considered to be an advantageous technology, since it utilizes sustainable solar light as well as abundantly available water resources. Additionally, the formation of harmless H_2O and CO_2 molecules as byproducts makes this technique environmentally friendly. MFGNs exhibit excellent performance for the photodegradation of organic dyes. For instance, a $ZnFe_2O_4$/rGO composite degraded MB 7.6 times more than pristine $ZnFe_2O_4$ under solar-light irradiation. The augmented photoactivity was attributed to the impeccable hybridization of GNs with the MFs. This review article depicts various synthesis protocols for the fabrication of MFGNs, focusing on their augmented dye-degradation performance and highlighting the possible photocatalytic-dye-detoxification mechanisms. An overview is presented in Scheme 5.

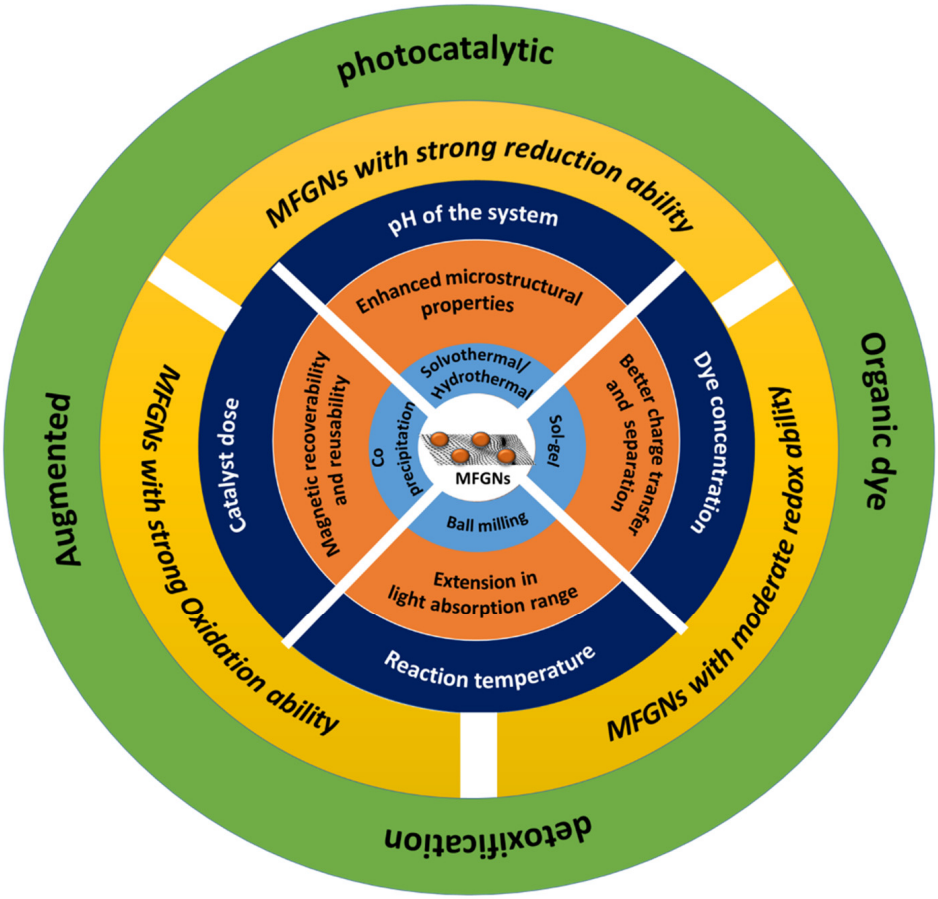

Scheme 5. A pictorial overview of photocatalytic-dye detoxification using MFGNs.

Synthesis strategies play an important role in modulating photoactivity through the optimization of crystallinity, particle size, and microstructural properties. A solvothermally synthesized $ZnFe_2O_4$/rGO nanocomposite retained the cubic structure of $ZnFe_2O_4$ along with an enhanced crystallinity. $CoFe_2O_4$/rGO nanocomposites prepared by the ball milling technique possessed 10–15 nm particles, which were uniformly distributed over exfoliated graphene sheets. These composite photocatalysts displayed excellent performance in contrast to their pristine counterparts.

The robust decoration of GNs with MFs caused a synergetic effect of the modified textural and microstructural properties, pronounced charge carriers' separation and migration, and an extended light-absorption range, with the composite photocatalysts displaying an exceptionally high dye-degradation efficiency. The integration of rGO with $CoFe_2O_4$ reduced the particle size to 49 nm. Similarly, rGO anchoring favored a decrease in the pore diameter of $ZnFe_2O_4$ from 12.4 nm to 5.2 nm and enhanced its surface area from 113.8 to 141.3 $m^2\ g^{-1}$. PL, EIS, and photocurrent studies revealed distinct isolation and increased

transportation of charge carriers. This elongated the life time of the charge carriers that are predominantly available at the MFGN surface, which improved the photodegradation of dyes. For example, the photocurrent response of $MnFe_2O_4$/graphene was found to be five times higher than that of the pristine one, as an indicative of the better separation of the photoinduced electron and hole pairs. It was also evident that GNs broaden the light-response range, when combined properly with MFs. A $CuFe_2O_4$/rGO photocatalyst showed an extended light response up to 800 nm. Moreover, parameters such as pH of solution, temperature, catalyst dose, and dye concentration greatly influence the dye-degradation reaction. The exceptional stability and facile recoverability experienced by MFGNs can be a major advantage in the support of their possible practical applications for dye degradation.

The enhanced photodegradation of dyes over MFGNs could be explained through three different mechanisms, depending on the redox ability of MFs. These are (i) MFGNs with a strong reduction ability, (ii) MFGNs with a strong oxidation ability, and (iii) MFGNs with a moderate redox ability. In the first case, strongly reactive OH free radicals are generated through the photo-Fenton process. The second mechanism proposes the release of OH free radicals directly by h^+-driven water-oxidation reactions. According to the third mechanism, reactive species such as OH and SO_4^- are produced through the photo-Fenton and PMS activation processes, respectively. These species with robust oxidizing abilities greatly detoxify the dye molecules.

By and large, MFGNs exhibited excellent photocatalytic activity for the degradation of organic dyes. However, this photocatalytic system faces a number of challenges for its practical applicability. These emerging challenges are addressed in this section, with the hope for possible solutions in the future. Despite prominent charge carriers' separation and migration owing to the robust integration of GN with MFs, the life span of the excitons on MFGNs are required to further increase in order to achieve desired photoactivity. Though MFGNs exhibited an extended light-absorption range compared to pristine MFs, the light-response window needs to be further widened to Near Infra-Red (NIR) region in order for the complete utilization of the solar spectrum. It is highly desirable to improve MFGNs' redox ability, which is essentially required for producing enough reactive species with a strong oxidizing ability to carry out the dye-degradation reaction efficiently. The pH of the photodegradation reaction should be neutrally maintained at pH = 7.0, for application in natural water bodies. Efforts may, therefore, be explored in the future to overcome these emerging challenges to enable the MFGNs' photocatalytic system to become a benchmark in the photodetoxification of dyes.

Future research directions may be shaped as follows, in order to obtain the desired MFGN systems for the efficient photocatalytic detoxification of dyes. Construction of ternary composites by integrating narrow band gap semiconductors with MFGN might be a timely strategy to extend the light-absorption range up to NIR, to harness the complete solar spectrum. Designing Z-scheme/S-scheme heterostructured architectures would enable MFGN systems with a robust redox ability as well as improved charge carriers' separation and migration. This would boost the efficiency of the present photocatalytic system, thus exhibiting a strong performance for the dye-detoxification process. Although operation of a photocatalytic-dye-decomposition reaction at natural pH is a strenuous task, the proper design of a photocatalytic system might produce a coveted solution for this problem. The emerging challenges and future research directions are depicted in Scheme 6. A cumulative effort from all quarters including scientists, researchers, and engineers will pragmatically assist to move MFGNs to the front line in the process of the complete detoxification of organic dyes through solar-induced photocatalysis. This will certainly shed light onto the survival of aquatic lives and downstream users in the future. We hope this review article will be helpful for researchers in understanding the concepts required to design an effective photocatalytic system for the complete removal of dyes from natural water bodies.

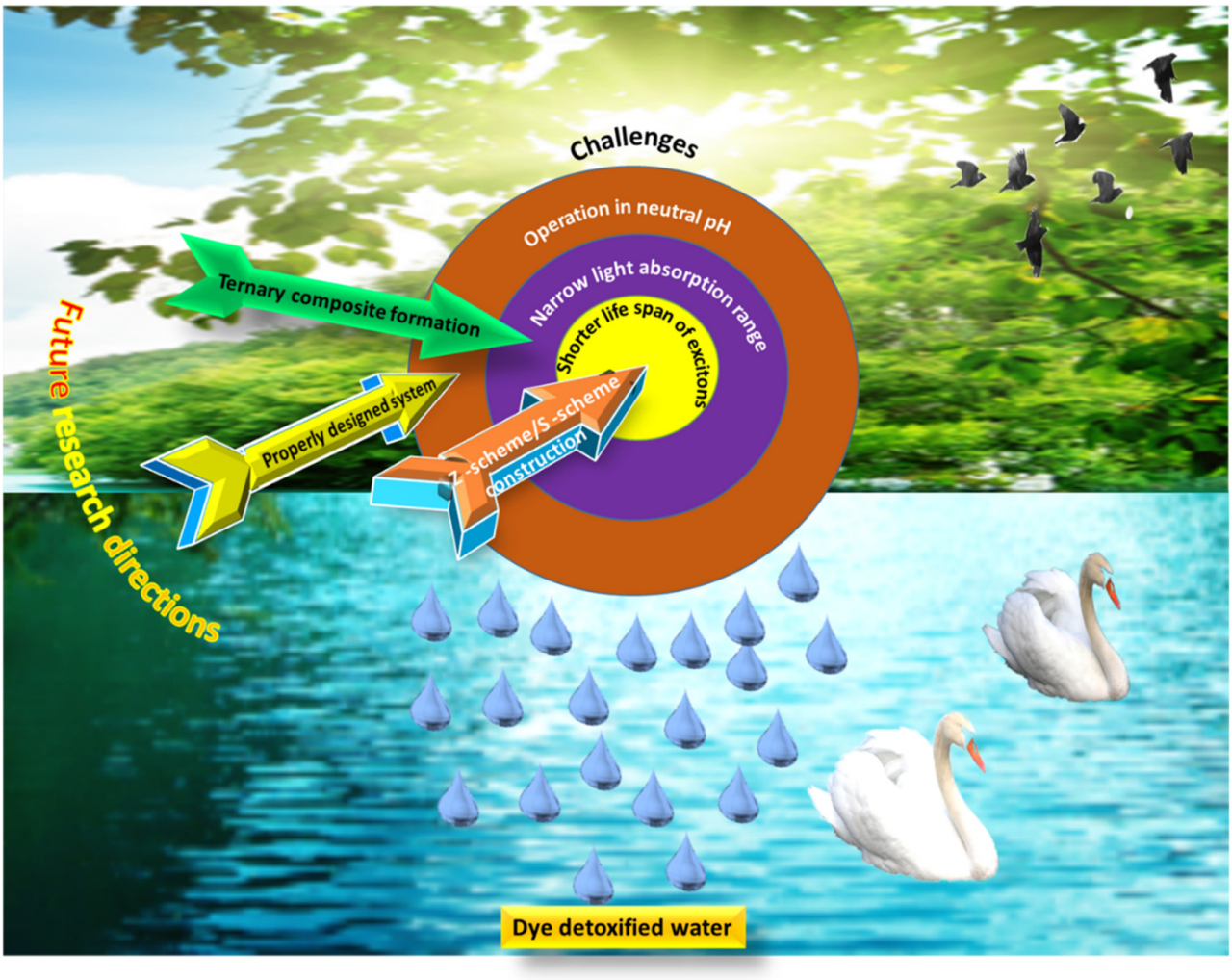

Scheme 6. Challenges and future research directions for the photodetoxification of dyes over MFGNs.

Author Contributions: S.M.: drafting of the manuscript; R.A.: drafting and editing of the manuscript; K.P.: checking of the manuscript. All authors have read and agreed to the published version of the manuscript.

Funding: The authors declare that no funds, grants, or other support were received during the preparation of this manuscript.

Data Availability Statement: Not applicable.

Acknowledgments: The authors express a deep sense of gratitude to the management of Siksha 'O' Anusandhan (Deemed to be University), Bhubaneswar, Odisha, India, for their constant support of the present work. Ashok Kumar Mohanty is thankfully acknowledged for the English corrections in the manuscript.

Conflicts of Interest: The authors have no relevant financial or non-financial interests to disclose.

References

1. Chen, C.; Ma, W.; Zhao, J. Semiconductor-mediated photodegradation of pollutants under visible-light irradiation. *Chem. Soc. Rev.* **2010**, *39*, 4206. [CrossRef] [PubMed]
2. Adeleke, J.T.; Theivasanthi, T.; Thiruppathi, M.; Swaminathan, M.; Akomolafe, T.; Alabi, A.B. Photocatalytic degradation of methylene blue by ZnO/$NiFe_2O_4$ nanoparticles. *Appl. Surf. Sci.* **2018**, *455*, 195–200. [CrossRef]
3. Rafiq, A.; Ikram, M.; Ali, S. Photocatalytic degradation of dyes using semiconductor photocatalysts to clean industrial water pollution. *J. Indust. Eng. Chem.* **2021**, *97*, 111–128. [CrossRef]
4. Katheresan, V.; Kansedo, J.; Lau, S.Y. Efficiency of various recent wastewater dye removal methods: A review. *J. Environ. Chem. Eng.* **2018**, *6*, 4676–4697. [CrossRef]

5. Ahmad, A.; Hamidah, S.; Mohd-Setapar, S.H.; Chuong, C.S.; Khatoon, A.; Wani, W.A.; Kumard, R.; Rafatullah, M. Recent advances in new generation dye removal technologies: Novel search for approaches to reprocess wastewater. *RSC Adv.* **2015**, *5*, 30801. [CrossRef]
6. Yagub, M.T.; Sen, T.K.; Afroze, S.; Ang, H.M. Dye and its removal from aqueous solution by adsorption: A review. *Adv. Colloid Interf. Sci.* **2014**, *209*, 172–184. [CrossRef]
7. Dutta, S.; Gupta, B.; Srivastava, S.K.; Gupta, A.K. Recent advances on the removal of dyes from wastewater using various adsorbents: A critical review. *Adv. Mater.* **2021**, *2*, 4497–4531. [CrossRef]
8. Pattnaik, S.P.; Behera, A.; Acharya, R.; Parida, K. Green exfoliation of graphitic carbon nitride towards decolourization of Congo-Red under solar irradiation. *J. Environ. Chem. Eng.* **2019**, *7*, 103456. [CrossRef]
9. Pattnaik, S.P.; Behera, A.; Martha, S.; Acharya, R.; Parida, K. Synthesis, photoelectrochemical properties and solar light-induced photocatalytic activity of bismuth ferrite nanoparticles. *J. Nanopart. Res.* **2018**, *20*, 10. [CrossRef]
10. Frank, S.N.; Bard, A.J. Heterogeneous photocatalytic oxidation of cyanide ion in aqueous solutions at TiO_2 powder. *J. Am. Chem. Soc.* **1977**, *99*, 303–304. [CrossRef]
11. Rauf, M.A.; Ashraf, S.S. Fundamental principles and application of heterogeneous photocatalytic degradation of dyes in solution. *Chem. Eng. J.* **2009**, *151*, 10–18. [CrossRef]
12. Friedmann, D. A General Overview of Heterogeneous Photocatalysis as a Remediation Technology for Wastewaters Containing Pharmaceutical Compounds. *Water* **2022**, *14*, 3588. [CrossRef]
13. Acharya, R.; Naik, B.; Parida, K. Cr(VI) remediation from aqueous environment through modified-TiO_2-mediated photocatalytic reduction. *Beilstein J. Nanotechnol.* **2018**, *9*, 1448–1470. [CrossRef] [PubMed]
14. Mansingh, S.; Sultana, S.; Acharya, R.; Ghosh, M.K.; Parida, K. Efficient photon conversion via double charge dynamics CeO_2–$BiFeO_3$ p–n heterojunction photocatalyst promising toward N_2 fixation and Phenol–Cr(VI) detoxification. *Inorg. Chem.* **2020**, *59*, 3856–3873. [CrossRef] [PubMed]
15. Lee, K.M.; Lai, C.W.; Ngai, K.S.; Juan, J.C. Recent developments of zinc oxide based photocatalyst in water treatment technology: A review. *Water Res.* **2015**, *88*, 428–448. [CrossRef] [PubMed]
16. Acharya, L.; Swain, G.; Mishra, B.P.; Acharya, R.; Parida, K. Development of $MgIn_2S_4$ microflower-embedded exfoliated B-doped g-C_3N_4 nanosheets: P–n heterojunction photocatalysts toward photocatalytic water reduction and H_2O_2 production under visible-light irradiation. *ACS Appl. Energy Mater.* **2022**, *5*, 2838–2852. [CrossRef]
17. Antoniadou, M.; Arfanis, M.K.; Ibrahim, I.; Falaras, P. Bifunctional g-C_3N_4/WO_3 thin films for photocatalytic water purification. *Water* **2019**, *11*, 2439. [CrossRef]
18. Lei, D.; Xue, J.; Peng, X.; Lia, S.; Bi, Q.; Tang, C. Oxalate enhanced synergistic removal of chromium(VI) and arsenic(III) over $ZnFe_2O_4$/g-C_3N_4: Z-scheme charge transfer pathway and photo-Fenton like reaction. *Appl. Catal. B.* **2021**, *282*, 119578. [CrossRef]
19. Jo, W.-K.; Moru, S.; Tonda, S. Magnetically responsive $SnFe_2O_4$/g-C_3N_4 hybrid photocatalysts with remarkable visible-light-induced performance for degradation of environmentally hazardous substances and sustainable hydrogen production. *Appl. Surf. Sci.* **2020**, *506*, 144939. [CrossRef]
20. Kefeni, K.K.; Msagatia, T.A.M.; Nkambule, T.T.; Mamba, B.B. Spinel ferrite nanoparticles and nanocomposites for biomedical applications and their toxicity. *Mater. Sci. Eng. C.* **2020**, *107*, 110314. [CrossRef]
21. Kefeni, K.K.; Mamba, B.B.; Msagatia, T.A.M. Application of spinel ferrite nanoparticles in water and wastewater treatment: A review. *Separ. Purif. Technol.* **2017**, *188*, 399–422. [CrossRef]
22. Xiang, Q.; Yu, J.; Jaroniec, M. Graphene-based semiconductor photocatalysts. *Chem. Soc. Rev.* **2012**, *41*, 782–796. [CrossRef]
23. Li, X.; Yu, J.; Wageh, S.; Al-ghamdi, A.A.; Xie, J. Graphene in Photocatalysis: A Review. *Small* **2016**, *12*, 6640. [CrossRef]
24. Yang, D.; Feng, J.; Jiang, L.; Wu, X.; Sheng, L.; Jiang, Y.; Wei, T.; Fan, Z. Photocatalyst interface engineering: Spatially confined growth of $ZnFe_2O_4$ within graphene networks as excellent visible-light-driven photocatalysts. *Adv. Funct. Mater.* **2015**, *25*, 7080–7087. [CrossRef]
25. Fu, Y.S.; Wang, X. Magnetically separable $ZnFe_2O_4$-graphene catalyst and its high photocatalytic performance under visible light irradiation. *Ind. Eng. Chem. Res.* **2011**, *50*, 7210–7218. [CrossRef]
26. Hou, Y.; Li, X.; Zhao, Q.; Chen, G. $ZnFe_2O_4$ multi-porous microbricks/graphene hybrid photocatalyst: Facile synthesis, improved activity and photocatalytic mechanism. *Appl. Catal. B* **2013**, *142–143*, 80–88. [CrossRef]
27. Behera, A.; Kandi, D.; Mansingh, S.; Martha, S.; Parida, K. Facile synthesis of $ZnFe_2O_4$@rGO nanocomposites towards photocatalytic ciprofloxacin degradation and H_2 energy production. *J. Coll. Interf. Sci.* **2019**, *556*, 667–679. [CrossRef]
28. Karim, K.M.R.; Tarek, M.; Ong, H.R.; Abdullah, H.; Yousuf, A.; Cheng, C.K.; Khan, M.M.R. Photoelectrocatalytic Reduction of Carbon Dioxide to Methanol Using $CuFe_2O_4$ Modified with Graphene Oxide under Visible Light Irradiation. *Ind. Eng. Chem. Res.* **2019**, *58*, 563–572. [CrossRef]
29. Mekasuwandumronga, O.; Pawinrat, P.; Praserthdamb, P.; Panpranot, J. Effects of synthesis conditions and annealing post-treatment on the photocatalytic activities of ZnO nanoparticles in the degradation of methylene blue dye. *Chem. Eng. J.* **2020**, *164*, 77–84. [CrossRef]
30. Fei, P.; Wang, Q.; Zhong, M.; Su, B. Preparation and adsorption properties of enhanced magnetic zinc ferrite-reduced graphene oxide nanocomposites via a facile one-pot solvothermal method. *J. Alloy. Compd.* **2016**, *685*, 411–417. [CrossRef]
31. Yin, W.; Haoab, S.; Cao, H. Solvothermal synthesis of magnetic $CoFe_2O_4$/rGO nanocomposites for highly efficient dye removal in wastewater. *RSC Adv.* **2017**, *7*, 4062. [CrossRef]

32. Hu, L.; Li, M.; Cheng, L.; Jiang, A. Solvothermal synthesis of octahedral and magnetic $CoFe_2O_4$–reduced graphene oxide hybrids and their photo-Fenton-like behavior under visible light irradiation. *RSC Adv.* **2021**, *11*, 22250. [CrossRef]
33. Meidanchi, A.; Akhavan, O. Superparamagnetic zinc ferrite spinel–graphene nanostructures for fast wastewater purification. *Carbon* **2014**, *69*, 230–238. [CrossRef]
34. Kumar, S.; Nair, R.R.; Pillai, P.B.; Gupta, S.N.; Iyengar, M.A.R.; Sood, A.K. Graphene oxide−$MnFe_2O_4$ magnetic nanohybrids for efficient removal of lead and arsenic from water. *ACS Appl. Mater. Interf.* **2014**, *6*, 17426–17436. [CrossRef] [PubMed]
35. Rostami, M.; Zamani, R.M.; Aghajanzadeh, K.M.; Danafar, H. Sol–gel synthesis and characterization of zinc ferrite–graphene nano-hybrids for photo-catalytic degradation of the paracetamol. *J. Pharm. Investig.* **2016**, *48*, 657–664. [CrossRef]
36. He, G.; Ding, J.; Zhang, J.; Hao, Q.; Chen, H. One-step ball-milling preparation of highly photocatalytic active $CoFe_2O_4$-reduced graphene oxide heterojunctions for organic dye removal. *Ind. Eng. Chem. Res.* **2015**, *54*, 2862–2867. [CrossRef]
37. Kumar, S.; Kumar, A.; Bahuguna, A.; Sharma, V.; Krishnan, V. Two-dimensional carbon-based nanocomposites for photocatalytic energy generation and environmental remediation applications. *Beilstein J. Nanotechnol.* **2017**, *8*, 1571–1600. [CrossRef]
38. Mansingh, S.; Acharya, R.; Martha, S.; Parida, K. Pyrochlore $Ce_2Zr_2O_7$ decorated over rGO: A photocatalyst that proves to be efficient towards the reduction of 4-nitrophenol and degradation of ciprofloxacin under visible light. *Phys. Chem. Chem. Phys.* **2018**, *20*, 9872–9885. [CrossRef]
39. Moussa, H.; Girot, E.; Mozet, K.; Alem, H.; Medjahdi, G.; Schneider, R. ZnO rods/reduced graphene oxide composites prepared via a solvothermal reaction for efficient sunlight-driven photocatalysis. *Appl. Catal. B.* **2016**, *185*, 11. [CrossRef]
40. Mahdikhah, V.; Saadatkia, S.; Sheibani, S.; Ataie, A. Outstanding photocatalytic activity of $CoFe_2O_4$ /rGO nanocomposite in degradation of organic dyes. *Opt. Mater.* **2020**, *108*, 110193. [CrossRef]
41. Baynosa, M.L.; Mady, A.H.; Nguyen, V.Q.; Kumar, D.R.; Sayed, M.S.; Tuma, D.; Shim, J.-J. Eco-friendly synthesis of recyclable mesoporous zinc ferrite @ reduced graphene oxide nanocomposite for efficient photocatalytic dye degradation under solar radiation. *J. Colloid Interface Sci.* **2020**, *561*, 459–469. [CrossRef] [PubMed]
42. Low, J.; Yu, J.; Jaroniec, M.; Wageh, S.; Al-Ghamdi, A.A. Heterojunction photocatalysts. *Adv. Mater.* **2017**, *29*, 1601694. [CrossRef] [PubMed]
43. Li, X.; Shen, R.; Ma, S.; Chen, X.; Xie, J. Graphene-based heterojunction photocatalysts. *Appl. Surf. Sci.* **2018**, *430*, 53–107. [CrossRef]
44. Liu, S.-Q.; Zhu, X.-L.; Zhou, Y.; Meng, Z.-D.; Chen, Z.-G.; Liu, C.-B.; Chen, F.; Wu, Z.-Y.; Qian, J.-C. Smart photocatalytic removal of ammonia through molecular recognition of zinc ferrite/reduced graphene oxide hybrid catalyst under visible-light irradiation. *Catal. Sci. Technol.* **2017**, *7*, 3210–3219. [CrossRef]
45. Mokhtar, M.; Islam, M.; Tarek, I.; Salama, M. Rational design of manganese ferrite-graphene hybrid photocatalysts: Efficient water splitting and effective elimination of organic pollutants. *Appl. Catal. A Gen.* **2016**, *524*, 182–191.
46. Nazim, S.; Kousar, T.; Shahid, M.; Khan, M.A.; Nasara, G.; Sher, M.; Warsia, M.F. New graphene-$Co_xZn_{1-x}Fe_2O_4$ nano-heterostructures: Magnetically separable visible light photocatalytic materials. *Ceram. Int.* **2016**, *42*, 7647–7654. [CrossRef]
47. Fu, Y.; Xiong, P.; Chen, H.; Sun, X.; Wang, X. High photocatalytic activity of magnetically separable manganese ferrite-graphene hetero-architectures. *Ind. Eng. Chem. Res.* **2012**, *51*, 725–731. [CrossRef]
48. Zhang, H.; Lv, X.; Li, Y.; Wang, Y.; Li, J. P25-graphene composite as a high performance photocatalyst. *ACS Nano* **2010**, *4*, 380–386. [CrossRef]
49. Mady, A.H.; Baynosa, M.L.; Tumac, D.; Shim, J.-J. Facile microwave-assisted green synthesis of Ag-$ZnFe_2O_4$@rGO nanocomposites for efficient removal of organic dyes under UV- and visible-light irradiation. *Appl. Catal. B* **2017**, *203*, 416–427. [CrossRef]
50. Soltani, T.; Lee, B.-K. Sono-synthesis of nanocrystallized $BiFeO_3$/reduced graphene oxide composites for visible photocatalytic degradation improvement of bisphenol A. *Chem. Eng. J.* **2016**, *306*, 204–213. [CrossRef]
51. Israr, M.; Iqbal, J.; Arshad, A.; Gomez-Romero, P. Sheet-on-sheet like calcium ferrite and graphene nanoplatelets nanocomposite: A multifunctional nanocomposite for high-performance supercapacitor and visible light driven photocatalysis. *J. Solid State Chem.* **2021**, *293*, 121646. [CrossRef]
52. Ai, J.; Hu, L.; Zhou, Z.; Cheng, L.; Liu, W.; Su, K.; Zhang, R.; Chen, Z.; Li, W. Surfactant-free synthesis of a novel octahedral $ZnFe_2O_4$/graphene composite with high adsorption and good photocatalytic activity for efficient treatment of dye wastewater. *Ceram. Int.* **2020**, *46*, 11786–11798. [CrossRef]
53. Liang, J.; Wei, Y.; Zhang, J.; Yao, Y.; He, G.; Tang, B.; Chen, H. Scalable green method to fabricate magnetically separable $NiFe_2O_4$-reduced graphene oxide nanocomposites with enhanced photocatalytic performance driven by visible light. *Ind. Eng. Chem. Res.* **2018**, *57*, 4311–4319. [CrossRef]
54. Moitra, D.; Chandel, M.; Ghosh, B.K.; Jani, R.K.; Patra, M.K.; Vadera, S.R.; Ghosh, N.N. A simple 'in situ' co-precipitation method for preparation of multifunctional $CoFe_2O_4$-reduced graphene oxide nanocomposites: Excellent microwave absorber and highly efficient magnetically separable recyclable photocatalyst for dye degradation. *RSC Adv.* **2016**, *6*, 76759–76772. [CrossRef]
55. Dong, J.; Chen, G.; Sun, J.; Li, C.; Yu, Y.; Chen, D. A novel high-efficiency visible-light sensitive Ag_2CO_3 photocatalyst with universal photodegradation performances: Simple synthesis, reaction mechanism and first-principles study. *Appl. Catal. B* **2013**, *134–135*, 46–54. [CrossRef]
56. Acharya, R.; Parida, K. A review on TiO_2/g-C_3N_4 visible-light- responsive photocatalysts for sustainable energy generation and environmental remediation. *J. Environ. Chem. Eng.* **2020**, *8*, 103896. [CrossRef]

57. Zou, L.; Wang, H.; Yuan, G.; Wang, X. Magnetically separable CdS/$ZnFe_2O_4$ composites with highly efficient photocatalytic activity and photostability under visible light. *ACS Appl. Nano Mater.* **2018**, *1*, 831–838. [CrossRef]
58. Costa, R.C.C.; Lelis, M.F.F.; Oliveira, L.C.A. Novel active heterogeneous Fenton system based on Fe3-xMxO4 (Fe, Co, Mn, Ni): The role of M^{2+} species on the reactivity towards H_2O_2 reactions. *J. Hazard. Mater. B* **2006**, *129*, 171–178. [CrossRef]
59. Sharma, R.; Bansal, S.; Singhal, S. Tailoring the photo- fenton activity of spinel ferrites (MFe_2O_4) by incorporating different cations ($M\frac{1}{4}$ Cu, Zn, Ni and Co) in the structure. *RSC Adv.* **2015**, *5*, 6006–6018. [CrossRef]
60. Chen, P.; Xing, X.; Xie, H.; Sheng, Q.; Qu, H. High catalytic activity of magnetic $CuFe_2O_4$/graphene oxide composite for the degradation of organic dyes under visible light irradiation. *Chem. Phys. Let.* **2016**, *660*, 176–181. [CrossRef]
61. Lu, D.; Zhang, Y.; Lin, S.; Wang, L.; Wang, C. Synthesis of magnetic $ZnFe_2O_4$/graphene composite and its application in photocatalytic degradation of dyes. *J. Alloys Compd.* **2013**, *579*, 336–342. [CrossRef]
62. Jiang, R.; Zhu, H.; Fu, Y.; Jiang, S.; Zong, E.; Yao, J. Photocatalytic decolorization of congo red wastewater by magnetic $ZnFe_2O_4$/graphene nanosheets composite under simulated solar light irradiation. *Ozone Sci. Eng.* **2020**, *42*, 174–182. [CrossRef]
63. Tamilselvi, R.; Lekshmi, G.S.; Padmanathan, N.; Selvaraj, V.; Bazaka, O.; Levchenko, I.; Bazaka, K.; Mandhakini, M. $NiFe_2O_4$/rGO nanocomposites produced by soft bubble assembly for energy storage and environmental remediation. *Renew. Energy* **2022**, *181*, 1386–1401. [CrossRef]
64. Rahman, A.; Warsia, M.F.; Shakir, I.; Shahid, M.; Zulfiqar, S. Fabrication of Ce^{3+} substituted nickel ferrite-reduced graphene oxide heterojunction with high photocatalytic activity under visible light irradiation. *J. Hazard. Mater.* **2020**, *394*, 122593. [CrossRef]
65. Wei, Z.; Huang, S.; Zhang, X.; Lu, C.; He, Y. Hydrothermal synthesis and photo-Fenton degradation of magnetic $MnFe_2O_4$/rGO nanocomposites. *J. Mater. Sci. Mater. Electron.* **2020**, *31*, 5176–5186. [CrossRef]
66. He, H.-Y.; Lu, J. Highly photocatalytic activities of magnetically separable reduced graphene oxide-$CoFe_2O_4$ hybrid nanostructures in dye photodegradation. *Sep. Purif. Technol.* **2017**, *172*, 374–381. [CrossRef]
67. Mazarji, M.; Esmaili, H.; Bidhendi, G.N.; Mahmoodi, N.M.; Minkina, T.; Sushkova, S.; Mandzhieva, S.; Barakhov, A.; Moghtaderi, H.; Bhatnagar, A. Green synthesis of reduced graphene oxide-$CoFe_2O_4$ nanocomposite as a highly efficient visible-light-driven catalyst in photocatalysis and photo Fenton-like reaction. *Mater. Sci. Eng. B* **2021**, *270*, 115223. [CrossRef]
68. Klamerth, N.; Malato, S.; Agüera, A.; Fernández-Alba, A.; Mailhot, G. Treatment of municipal wastewater treatment plant effluents with modified photo-fenton as a tertiary treatment for the degradation of micro pollutants and disinfection. *Environ. Sci. Technol.* **2012**, *46*, 2885–2892. [CrossRef]
69. Guan, Y.-H.; Ma, J.; Ren, Y.-M.; Liu, Y.-L.; Xiao, J.-Y.; Lin, L.-Q.; Zhang, C. Efficient degradation of atrazine by magnetic porous copper ferrite catalyzed peroxymonosulfate oxidation via the formation of hydroxyl and sulfate radicals. *Water Res.* **2013**, *47*, 5431–5438. [CrossRef]
70. Ren, F.; Zhu, W.; Zhao, J.; Liu, H.; Zhang, X.; Zhang, H.; Zhu, H.; Peng, Y.; Wang, B. Nitrogen-doped graphene oxide aerogel anchored with spinel $CoFe_2O_4$ nanoparticles for rapid degradation of tetracycline. *Sep. Purif. Technol.* **2020**, *241*, 116690. [CrossRef]
71. Zhang, Y.; Cheng, Y.; Qi, H. Synergistic degradation of organic pollutants on $CoFe_2O_4$/rGO nanocomposites by peroxymonosulfate activation under LED irradiation. *Appl. Surf. Sci.* **2022**, *579*, 152151. [CrossRef]
72. Fu, Y.; Chen, H.; Sun, X.; Wang, X. Combination of cobalt ferrite and graphene: High-performance and recyclable visible-light photocatalysis. *Appl. Catal. B Environ.* **2012**, *111–112*, 280–287. [CrossRef]
73. Zhang, D.; Wang, Q.; Wang, L.; Zhang, L. Magnetically separable $CdFe_2O_4$/graphene catalyst and its enhanced photocatalytic properties. *J. Mater. Chem. A* **2015**, *3*, 3576–3585. [CrossRef]
74. Yao, Y.; Cai, Y.; Lu, F.; Wei, F.; Wang, X.; Wang, S. Magnetic recoverable $MnFe_2O_4$ and $MnFe_2O_4$-graphene hybrid as heterogeneous catalysts of peroxymonosulfate activation for efficient degradation of aqueous organic pollutants. *J. Hazard. Mater.* **2014**, *270*, 61–70. [CrossRef] [PubMed]
75. Cai, H.; Zou, J.; Lin, J.; Lia, J.; Huang, H.; Zhang, S.; Yuan, B.; Ma, J. Sodium hydroxide-enhanced acetaminophen elimination in heat/peroxymonosulfate system: Production of singlet oxygen and hydroxyl radical. *Chem. Eng. J.* **2022**, *429*, 132438. [CrossRef]
76. Lin, J.; Zou, J.; Cai, H.; Huang, Y.; Li, J.; Xiao, J.; Yuan, B.; Ma, J. Hydroxylamine enhanced Fe(II)-activated peracetic acid process for diclofenac degradation: Efficiency, mechanism and effects of various parameters. *Water Res.* **2021**, *207*, 117796. [CrossRef]
77. Huang, Y.; Zou, J.; Lin, J.; Yang, H.; Wang, M.; Li, J.; Cao, W.; Yuan, B.; Ma, J. ABTS as Both Activator and Electron Shuttle to Activate Persulfate for Diclofenac Degradation: Formation and Contributions of ABTS•$^+$, SO4•$^-$, and •OH. *Environ. Sci. Technol.* **2022**. [CrossRef]
78. Huang, Y.; Lin, Y.; Zou, J.; Xu, J.; Wang, M.; Cai, H.; Yuan, B.; Ma, J. ABTS as an electron shuttle to accelerate the degradation of diclofenac with horseradish peroxidase-catalyzed hydrogen peroxide oxidation. *Sci. Total Environ.* **2021**, *798*, 149276. [CrossRef]
79. Daneshvar, N.; Salari, D.; Khataee, A.R. Photocatalytic degradation of azo dye acid red 14 in water: Investigation of the effect of operational parameters. *J. Photochem. Photobiol. A* **2003**, *157*, 111–116. [CrossRef]
80. You-ji, L.; Wei, C. Photocatalytic degradation of rhodamine B using nanocrystalline TiO_2–zeolite surface composite catalysts: Effects of photocatalytic condition on degradation efficiency. *Catal. Sci. Technol.* **2011**, *1*, 802–809. [CrossRef]
81. Bayantong, A.R.B.; Shih, Y.-J.; Dong, C.D.; Garcia-Segura, S.; Luna, M.D.G. Nickel ferrite nanoenabled graphene oxide ($NiFe_2O_4$@GO) as photoactive nanocomposites for water treatment. *Environ Sci. Pollut. Res.* **2020**, *28*, 5472–5481. [CrossRef] [PubMed]

82. Mozia, S.; Morawski, A.W.; Toyoda, M.; Tsumura, T. Effect of process parameters on photodegradation of Acid Yellow 36 in a hybrid photocatalysis–membrane distillation system. *Chem. Eng. J.* **2009**, *150*, 152. [CrossRef]
83. Kodasma, R.; Palas, B.; Ersöz, G.; Atalay, S. Photocatalytic activity of copper ferrite graphene oxide particles for an efficient catalytic degradation of Reactive Black 5 in water. *Ceram. Int.* **2020**, *46*, 6284–6292. [CrossRef]
84. Krishnan, S.; Murugesan, S.; Vasanthakumar, V.; Priyadharsan, A.; Alsawalha, M.; Alomayri, T.; Yuan, B. Facile green synthesis of $ZnFe_2O_4$/rGO nanohybrids and evaluation of its photocatalytic degradation of organic pollutant, photo antibacterial and cytotoxicity activities. *Colloids Surf. A: Physicochem. Eng. Asp.* **2021**, *611*, 125835.
85. Xu, L.; Wang, J. Magnetic nanoscaled Fe_3O_4/CeO_2 composite as an efficient Fenton-like heterogeneous catalyst for degradation of 4-chlorophenol. *Environ. Sci. Technol.* **2012**, *46*, 10145–10153. [CrossRef]
86. Lu, H.; Salabas, E.E.; Schüth, F. Magnetic nanoparticles: Synthesis, protection, functionalization, and application. *Angew. Chem. Int. Ed.* **2007**, *46*, 1222–1244. [CrossRef]
87. Gan, L.; Shang, S.; Wah, C.; Yuen, M.; Jiang, S.-X.; Hu, E. Hydrothermal synthesis of magnetic $CoFe_2O_4$/graphene nanocomposites with improved photocatalytic activity. *Appl. Surf. Sci.* **2015**, *351*, 140–147. [CrossRef]
88. Rani, G.J.; Jothirajan, M.A.; Gnanakumar, G. Reduced graphene oxide/$ZnFe_2O_4$ nanocomposite as an efficient catalyst for the photocatalytic degradation of methylene blue dye. *Res. Chem. Intermed.* **2017**, *43*, 2669–2690. [CrossRef]
89. Mandal, B.; Panda, J.; Paul, P.K.; Sarkar, R.; Tudu, B. $MnFe_2O_4$ decorated reduced graphene oxide heterostructures: Nanophotocatalyst for methylene blue dye degradation. *Vacuum* **2019**, *173*, 109150. [CrossRef]
90. Rahman, A.; Aadil, M.; Akhtar, M.; Warsi, M.F.; Jamil, A.; Shakir, I.; Shahid, M. Magnetically recyclable $Ni_{1-x}Cd_xCe_yFe_{2-y}O_4$-rGO nanocomposite photocatalyst for visible light driven photocatalysis. *Ceram. Int.* **2020**, *46*, 13517–13526. [CrossRef]